NASA/CR–2010-216700

Predicting Failure Progression and Failure Loads in Composite Open-Hole Tension Coupons

Arunkumar Satyanarayana
ATK Space Systems, Inc., Hampton, Virginia

Adam Przekop
Analytical Services & Materials, Inc., Hampton, Virginia

May 2010

NASA STI Program . . . in Profile

Since its founding, NASA has been dedicated to the advancement of aeronautics and space science. The NASA scientific and technical information (STI) program plays a key part in helping NASA maintain this important role.

The NASA STI program operates under the auspices of the Agency Chief Information Officer. It collects, organizes, provides for archiving, and disseminates NASA's STI. The NASA STI program provides access to the NASA Aeronautics and Space Database and its public interface, the NASA Technical Report Server, thus providing one of the largest collections of aeronautical and space science STI in the world. Results are published in both non-NASA channels and by NASA in the NASA STI Report Series, which includes the following report types:

- TECHNICAL PUBLICATION. Reports of completed research or a major significant phase of research that present the results of NASA programs and include extensive data or theoretical analysis. Includes compilations of significant scientific and technical data and information deemed to be of continuing reference value. NASA counterpart of peer-reviewed formal professional papers, but having less stringent limitations on manuscript length and extent of graphic presentations.

- TECHNICAL MEMORANDUM. Scientific and technical findings that are preliminary or of specialized interest, e.g., quick release reports, working papers, and bibliographies that contain minimal annotation. Does not contain extensive analysis.

- CONTRACTOR REPORT. Scientific and technical findings by NASA-sponsored contractors and grantees.

- CONFERENCE PUBLICATION. Collected papers from scientific and technical conferences, symposia, seminars, or other meetings sponsored or co-sponsored by NASA.

- SPECIAL PUBLICATION. Scientific, technical, or historical information from NASA programs, projects, and missions, often concerned with subjects having substantial public interest.

- TECHNICAL TRANSLATION. English-language translations of foreign scientific and technical material pertinent to NASA's mission.

Specialized services also include creating custom thesauri, building customized databases, and organizing and publishing research results.

For more information about the NASA STI program, see the following:

- Access the NASA STI program home page at *http://www.sti.nasa.gov*

- E-mail your question via the Internet to help@sti.nasa.gov

- Fax your question to the NASA STI Help Desk at 443-757-5803

- Phone the NASA STI Help Desk at 443-757-5802

- Write to:
  NASA STI Help Desk
  NASA Center for AeroSpace Information
  7115 Standard Drive
  Hanover, MD 21076-1320

NASA/CR–2010-216700

Predicting Failure Progression and Failure Loads in Composite Open-Hole Tension Coupons

Arunkumar Satyanarayana
ATK Space Systems, Inc., Hampton, Virginia

Adam Przekop
Analytical Services & Materials, Inc., Hampton, Virginia

National Aeronautics and
Space Administration

Langley Research Center
Hampton, Virginia 23681-2199

Prepared for Langley Research Center
under Contract NNL07AA00B

May 2010

Acknowledgments

The authors wish to thank Dawn C. Jegley and Dr. Cheryl A. Rose from the Structural Mechanics and Concepts branch at NASA Langley Research Center, Hampton, Virginia for their technical advice throughout the duration of the program and for their helpful comments during the preparation of this report.

Available from:

NASA Center for AeroSpace Information
7115 Standard Drive
Hanover, MD 21076-1320
443-757-5802

Table of Contents

List of Figures

List of Tables

Acronyms

2D	Two Dimensional
3D	Three Dimensional
COSTR	Complete Stress Reduction
DOF	Degree of Freedom
PFA	Progressive Failure Analysis

Symbols

d	damage coefficient
E	Young's modulus
G	Kirchoff's (shear) modulus
K	cohesive layer stiffness
l	length
N	number of elements in the cohesive zone
P	load
Q	lamina reduced stiffness matrix coefficient
S	lamina in-plane shear strength
t	thickness
U	inter-laminar strength
X	lamina strength in fiber direction
Y	lamina strength in transverse direction
α	numerical constant used in cohesive layer stiffness calculation
ε	strain
ν	Poisson's ratio
σ	stress

Subscripts:

I, II, III	crack mode
c	compression
e	element
f	fiber
i	first material directional index
j	second material directional index
M	matrix
m	number of stacks
n	number of layers
s	symmetric
t	tension

Abstract

Failure types and failure loads in carbon-epoxy $[45_n/90_n/-45_n/0_n]_{ms}$ laminate coupons with central circular holes subjected to tensile load are simulated using progressive failure analysis (PFA) methodology. The progressive failure methodology is implemented using VUMAT subroutine within the ABAQUS™/Explicit nonlinear finite element code. The degradation model adopted in the present PFA methodology uses an instantaneous complete stress reduction (COSTR) approach to simulate damage at a material point when failure occurs. In-plane modeling parameters such as element size and shape are held constant in the finite element models, irrespective of laminate thickness and hole size, to predict failure loads and failure progression. Comparison to published test data indicates that this methodology accurately simulates brittle, pull-out and delamination failure types. The sensitivity of the failure progression and the failure load to analytical loading rates and solvers' precision is demonstrated.

1.0 Introduction

Use of composite laminates in primary aerospace structures is rapidly increasing due to their high strength, low weight, ability to manufacture complex geometries and other factors. The strength and failure type of composite laminates are essential information required by engineers to design structures to meet safety requirements. Of particular interest are structural components with discontinuities (e.g., cutouts, holes, etc.). Over the past several years many researchers have embarked on developing progressive failure analysis (PFA) methodologies to predict failure loads and damage modes in composites [1–23]. However, the reliability of these methodologies in analyzing typical aerospace structural components needs to be improved.

The PFA methodology development is a complex task resulting in significant challenges at several steps of the procedure. One such step, which is also an active research area in PFA methodology development, is defining degradation models for adjusting material properties or stresses to simulate damage modes such as fiber, matrix and inter-laminar (delamination) failures. Identifying material properties or stresses to degrade for the given damage modes, and the rates of degradation themselves, are all part of ongoing research. The PFA methodologies and the damage models which are commonly used to predict the in-plane damage modes and the failure loads are very well summarized in Refs. 1, and 13. Most of the in-plane damage models are successful in predicting fiber and matrix failure in most laminate sequences where the through-thickness crack propagates in a self-similar fashion (i.e., perpendicular to the loading direction). Another factor which makes the PFA methodology less reliable is its dependency on the element size for accurate solution predictions. Dependency of the failure load predictions on the element size is a well known phenomenon. Researchers in Refs. 13–14 attempted to address this issue by equating the fracture energy of the material to the energy dissipation due to the damage mode. As indicated in Ref. 14, fracture properties of the fiber may not be as readily available as other standard material properties.

To compensate for the lack of maturity of PFA methodology and also to generate test data to support its development and validation efforts, several experimental investigations were conducted in the recent past. Among test results published in the literature, Green et al. [24] reported on their tests conducted on the composite tension coupons with a centrally located hole. Three distinct failure types were observed in the test. Based on the post-failure examination of the specimens, the failure types were

characterized as brittle, pull-out and delamination, and were shown to be dependent upon the diameter of the hole, the laminate thickness and the stacking sequence. These unique failure types were triggered by one of the in-plane stresses reaching the failure limit ahead of the others. Since the test results published by Green at al. [24] covered all the three known failure types, they were selected as an attractive and comprehensive ground for the validation effort of the PFA methodology used in the current study.

The objective of the current work was to examine the capabilities of the previously developed in-plane damage models [12, 19] and the modeling procedures in predicting the failure load and the failure types of the open-hole tension specimens. Simulation of complex failure types, such as the ones shown in the experimental work by Green et al. [24], requires both intra-laminar and inter-laminar damage models applied simultaneously. This is a challenging task that tests the limits of the damage models. The detection of intra-laminar damage was accomplished using the Hashin-Rotem failure criteria [25–27]. The intra-laminar modeling parameters, such as the in-plane mesh size and its orientation around the discontinuous regions, were maintained approximately constant for all the coupons analyzed in this study and are described in the finite element model development section. The explanation of the degradation technique and the damage model used in the current study are presented in the following sections. The damage model with failure criteria for PFA was implemented using user-written material modeling subroutine (VUMAT) in the ABAQUS™ finite element analysis code and its explicit nonlinear solver was used in the simulation. The inter-laminar damage mode (delamination) was simulated using cohesive zone model [28–30] in ABAQUS™. The inter-laminar modeling procedure for the cohesive layers is explained in the finite element model development section of this report.

In the current study, PFAs of 8-, 16- and 32-ply laminates with a 0.25-inch and 0.5-inch-diameter hole located at the center were performed. A 32-ply laminate with a 0.5-inch-diameter hole located at the center, but scaled in such a way as to not group same-direction plies together, was also analyzed. Results such as failure loads and the failure types of these laminates obtained from the PFA are presented in tabular and pictorial forms showing the inter-laminar and the intra-laminar damage modes and their corresponding loads. Numerical results, such as failure stress, are compared with the test data provided in Ref. 24. The detailed description of the failure types exhibited by these laminates, as explained in Ref. 24, is compared with the simulated solutions obtained from the PFA.

In this study, the ABAQUS™/Explicit solver was used to solve a dynamic equation of motion. As application of very slow experimental loading rates of the coupons is impractical in the explicit analysis, an accelerated loading rate was applied. Therefore, the loading rate of the coupons in the analysis became an important factor. As a result, the influence of the loading rate and the application of ABAQUS™/Explicit single versus double precision solvers on the failure load, the failure types, and the sub-critical damages around the notch were examined.

2.0 Progressive Failure Analysis Methodology

PFA methodology consists of damage detection, damage evolution, and crack simulation. Damage detection is accomplished through the use of failure criteria for fiber and matrix failures. Both intra-laminar and the inter-laminar failure mechanisms were considered in the current PFA methodology. The damage evolution step of the PFA methodology consists of degrading the material properties or the stresses to a predetermined level or zero; and their rate of degradation depends on the hypothesis arrived at by the developers of the damage models.

2.1 In-Plane Damage Detection, Degradation Model and Damage Evolution

The Hashin-Rotem unidirectional failure criteria [26] are used to detect the fiber and matrix damage in a lamina. The ply stresses in the principal material directions are used in the unidirectional failure criteria. The failure criteria are expressed in terms of the in-plane stresses σ_{ij}, the strengths X and Y, and the shear strength S. The in-plane stresses σ_{11}, σ_{22}, and σ_{12}, are aligned with the principle material coordinate system in the ply. The strengths parallel and transverse to the fiber direction are denoted as X and Y, respectively. The in-plane shear strength is denoted as S_{12}. The subscripts c and t denote compression and tension, respectively. In the current study, the *in-situ* strengths are used for Y_t, and S_{12}, as per Ref. 31. The fiber failure indices in tension and compression are defined as

$$\begin{aligned} \left(\frac{\sigma_{11}}{X_t}\right) &\geq 1.0, \text{ then } d_f = 1 \text{ for } \sigma_{11} > 0 \\ \left(\frac{\sigma_{11}}{X_c}\right) &\geq 1.0, \text{ then } d_f = 1 \text{ for } \sigma_{11} < 0 \end{aligned} \tag{1}$$

The matrix failure indices in tension and compression are defined as

$$\begin{aligned} \left(\frac{\sigma_{22}}{Y_t}\right)^2 + \left(\frac{\sigma_{12}}{S_{12}}\right)^2 &\geq 1.0, \text{then } d_M = 1 \text{ for } \sigma_{22} > 0 \\ \left(\frac{\sigma_{22}}{Y_c}\right)^2 + \left(\frac{\sigma_{12}}{S_{12}}\right)^2 &\geq 1.0, \text{then } d_M = 1 \text{ for } \sigma_{22} < 0 \end{aligned} \tag{2}$$

Traditionally, in PFA methodology, damage is simulated by degrading the material properties [1] either instantaneously or gradually over several solution increments. The latter approach is used in many of the damage models to avoid numerical convergence issues [13, 14]. However, in the damage model presented herein, the terms in the constitutive matrix are instantaneously degraded to zero using damage parameters. The constitutive stress-strain relationship with the damage parameters for a two-dimensional (2D) orthotropic material can be written as

$$\begin{Bmatrix} \sigma_{11} \\ \sigma_{22} \\ \sigma_{12} \end{Bmatrix} = \begin{bmatrix} (1-d_f)Q_{11} & (1-d_f)(1-d_M)Q_{12} & 0 \\ (1-d_f)(1-d_M)Q_{12} & (1-d_f)(1-d_M)Q_{22} & 0 \\ 0 & 0 & (1-d_f)(1-d_M)Q_{66} \end{bmatrix} \begin{Bmatrix} \varepsilon_{11} \\ \varepsilon_{22} \\ \varepsilon_{12} \end{Bmatrix} \tag{3}$$

where

$$\begin{aligned} Q_{11} &= \frac{E_1}{(1-(1-d_M)\nu_{12}\nu_{21})} \\ Q_{12} &= \frac{\nu_{12}E_2}{(1-(1-d_M)\nu_{12}\nu_{21})} \\ Q_{22} &= \frac{E_2}{(1-(1-d_M)\nu_{12}\nu_{21})} \\ Q_{66} &= G_{12} \end{aligned} \tag{4}$$

where d_f and d_M are the damage parameters associated with the fiber and matrix failure modes, respectively. Each parameter has values of either 0 (no damage) or 1.0 (complete damage). In the above damage model, failure of the matrix, either due to the transverse or the shear stresses, causes simultaneous degradation of both these stresses. However, when the fiber fails, all of the stress components (i.e., axial, transverse and shear) are degraded instantaneously to zero. This damage model, which falls under the ply-discounting approach [1], is formulated considering the stress components associated with the fiber and matrix. Since the matrix in a composite material is associated with the transverse and shear stresses and the fiber is associated with the axial stress, when the damage is detected in the fiber or in the matrix all of the terms in the constitutive matrix corresponding to these stresses are completely reduced to zero instantaneously. From here on, this damage model is referred to as complete stress reduction (COSTR) model.

The in-plane damage evolution approach adopted in the present PFA methodology is based on the ply-degradation approach. In this approach, when fiber damage or matrix damage is detected at a material point, the corresponding damage parameter, d_f and d_M, respectively, changes instantaneously from 0 (undamaged state) to 1.0 (damaged state). From the constitutive equations of the COSTR damage model, Equations (3) and (4), it can be noticed that when the damage parameter d_M attains a value of 1.0 both the transverse and the shear stresses become zero. Similarly, when the damage parameter d_f attains a value of 1.0, all the in-plane stresses become zero. This type of instantaneous stress degradation to zero, which is accomplished via the damage parameters, is characterized as a single-step or instantaneous degradation approach [1]. Another characteristic of the COSTR damage model is the complete elimination of the influence of Poisson's ratio (ν) in evaluating the axial stress when the matrix has failed due to transverse or the shear stress.

In the current progressive failure methodology, the cracks (accumulation of fiber and matrix failures) in the laminates are simulated by application of the DELETE parameter available in the VUMAT routine. This simulation is accomplished by flagging a material point for deletion when the fiber has failed or when the transverse and/or shear strains reach 25 percent. It has been observed in some plies of the laminate, depending upon the loading conditions, that the transverse and/or shear strains could reach a significant level causing excessive distortion of the element without being stressed significantly in the fiber direction. An example of this phenomenon could be noticed in a laminate consisting of 90° plies and loaded in the direction perpendicular to the fiber. To avoid excessive distortion of the element due to large strains in the matrix, the quadratic strain criteria involving transverse and shear strains are formulated and implemented in the damage evolution procedure of the PFA methodology. Once a material point has been deleted, it cannot be reactivated. The ABAQUS™/Explicit solver checks for elements where all of the material points have been flagged as deleted and removes these elements from further computations, there by simulating virtual cracks in the finite element models. The failure detection criteria, COSTR damage model, and the element removal procedure are all implemented using a user-written subroutine VUMAT [30].

2.2 Inter-Laminar Damage Model

Inter-laminar damage, or delamination, initiation and progression are simulated by placing cohesive elements at potential delamination sites. The interface between the sub-laminates is modeled as a zero-thickness cohesive layer and discretized using COH3D8 elements [30]. The cohesive zone model[1] is used to simulate delamination. The onset of delamination is determined based on the inter-laminar quadratic nominal stress criterion and the delamination growth is based on a critical fracture energy criterion. Damage is modeled as an irreversible process by including a damage parameter [28-30]. This

[1]The cohesive zone model is based on a continuum-damage-mechanics formulation of a traction-displacement constitutive law for a thin resin layer that exists between adjacent composite lamina

damage parameter is directly related to the dissipated fracture energy. A detailed explanation of the cohesive zone model can be found in Refs. 28–30. The guidelines presented in Ref. 32 have been used to determine cohesive layer parameters such as element size, stiffnesses, and the interfacial strengths of the interface (cohesive layer) between the plies. The equation presented in Ref. 32 to define the stiffness of the cohesive layer in the mode-I direction is defined below as

$$K_I \approx \left(\frac{\alpha E_3}{t} \right) \tag{5}$$

where E_3 is the Young's modulus of the laminate in the thickness direction, t is the larger of the sub-laminate thicknesses above or below the cohesive layer, and α is a parameter that is much larger than 1. A value of α equal to 50 is recommended in Ref. 32 and was used in the current study to obtain a stiffness of the cohesive layer which is small enough to avoid numerical problems, such as spurious oscillations of the tractions in an element, and also large enough to prevent the laminate from being too compliant in the thickness direction. In calculating the stiffness K_{II} and K_{III} in the shear directions (mode-II and mode-III directions), E_3 is replaced with the shear moduli G_{12} and G_{13} of the laminate, respectively.

Interfacial strengths required to detect the onset of delamination are determined based on the in-plane element size of the cohesive layer, the fracture toughness of the material, and the number of elements in the cohesive zone using the following equation for mode-I failure:

$$U_I = \sqrt{\frac{9\pi E_3 G_I}{32 N_e l_e}} \tag{6}$$

where U_I is the inter-laminar strength in the mode-I direction, G_I is the corresponding fracture toughness, N_e is the user defined number of elements in the cohesive zone, and l_e is the length of the finite element in the cohesive layer [32]. The other interfacial strengths, U_{II} and U_{III}, are computed in the mode-II and mode-III directions by replacing G_I in Equation 4 with the G_{II} and G_{III} respectively.

Failed cohesive elements do not offer any resistance to the three inter-laminar opening modes. Hence, in the current study, when the failures of the cohesive elements occur, they are not deleted from the finite element model in order to prevent penetration of sub-laminate sections.

3.0 Problem Definition

The ability of the COSTR damage model and the PFA methodology to simulate failure loads and failure types is tested by analyzing the quasi-isotropic laminate coupons with a centrally located hole. This problem was of particular interest as it was experimentally investigated by Green et al. [24] and has demonstrated the effect of scaling and the through-the-thickness scaling approach on the failure type. A schematic diagram of the specimen tested is presented in Figure 3.1. These laminates were tested under quasi-static tension load. The dimension of the specimen, such as the width and length, were tied to the diameter of the hole. Multipliers of 5 and 20 were used for the width-to-hole diameter and the length-to-hole diameter ratios, respectively.

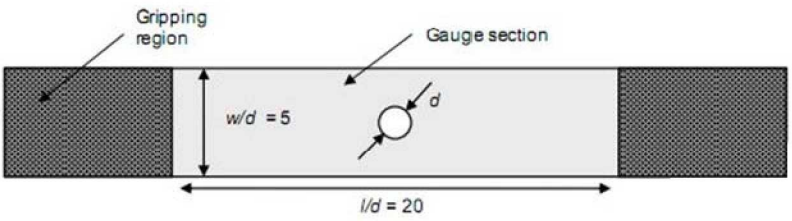

Figure 3.1. Schematic diagram of quasi-isotropic laminate coupon with centrally located hole [24].

Two hole diameters, 0.25 inches and 0.5 inches, were adopted with the laminate stacking sequence of $[45_n/90_n/-45_n/0_n]_s$ (the subscripts *n* refer to the number of plies for which values of 1, 2, or 4 were chosen and the subscript *s* refers to symmetry). For the laminate with a stacking sequence of $[45/90/-45/0]_{4s}$, only a 0.5-inch-diameter hole located at the center was analyzed. All of the specimens were made of IM7/8552 material. The material properties of IM7/8552 are provided in Table 3.1 [13]. The interfacial properties of the laminate, strain energy release rates and *in-situ* transverse tension, and in-plane shear strengths in the sub-laminate sections are presented in Table 3.2. The laminate stacking sequences and their thickness are presented in Table 3.3.

Table 3.1. IM7/8552 material properties.

E_{11} $\times 10^6$ psi	E_{22} $\times 10^6$ psi	G_{12} $\times 10^6$ psi	X_t $\times 10^6$ psi	X_c $\times 10^6$ psi	Y_t $\times 10^6$ psi	Y_c $\times 10^6$ psi	S_{12} $\times 10^6$ psi	ν_{12}
24.85	1.316	0.765	0.3373	0.1740	0.00899	0.28970	0.01888	0.32

Table 3.2. Fracture energies, inter-laminar strength and *in-situ* strength of IM7/8552 material.

G_I in-lbs/in^2	G_{II} in-lbs/in^2	G_{III} in-lbs/in^2	U_I $\times 10^6$ psi	U_{II} $\times 10^6$ psi	U_{III} $\times 10^6$ psi	Thick Embedded Plies		Thick Outer Plies	
						Y_t $\times 10^6$ psi	S $\times 10^6$ psi	Y_t $\times 10^6$ psi	S $\times 10^6$ psi
1.582	4.50	4.50	0.00678	0.01144	0.01144	0.01431	0.01660	0.01185	0.01344

Table 3.3. Laminate stacking sequences and thicknesses.

Number of Plies	8	16	32	32
Stacking Sequence	$[45/90/-45/0]_s$	$[45_2/90_2/-45_2/0_2]_s$	$[45_4/90_4/-45_4/0_4]_s$	$[45/90/-45/0]_{4s}$
Thickness, inches	0.0378	0.0772	0.1666	0.1666

3.1 Finite Element Model Description

Three-dimensional (3D) finite element models of seven specimen configurations[2] were developed to simulate coupled inter- and intra-laminar damage progression. The thickness of each model was divided into seven sub-laminate sections (0° layers in the middle of the laminates are modeled using one sub-laminate section) with a cohesive layer of zero thickness between each of them. The actual finite element model is shown in Figure 3.2 (a) and the pictorial representation of the modeling procedure in building sub-laminate sections and the cohesive layers of the laminates are shown in Figure 3.2 (b). The sub-laminate sections were discretized in the in-plane directions using a 0.09-inch × 0.09-inch 8-node continuum shell reduced integration element (SC8R) available in the ABAQUS™ element library [30]. The SC8R element is a 3D element with translational degrees-of-freedom (DOF) using only linear interpolation functions. It employs layer-wise composite theory and, unlike the conventional shell elements, it provides an ability to discretize 3D bodies It allows for mechanical and thermal loadings for static and dynamic solution procedures. The element size used in discretizating the sub-laminates is based on the conclusion of our previous work in which a finite element mesh sensitivity study was conducted to determine the approximate element size that would predict failure load of the notched laminate specimen close to the experimentally determined failure load for varying material systems and laminate thicknesses. The cohesive layers were modeled using a zero thickness ABAQUS™ 8-node cohesive element known as COH3D8 [30]. An in-plane discretization of 0.02 × 0.02 inches was used in the cohesive layers. The sub-laminate sections and the cohesive layers were connected using ABAQUS™ "tie" boundary conditions to maintain the continuity between the sub-laminate sections before the damage occurs. The assemblage of the seven sub-laminate sections and six cohesive layers through the thickness defines the complete laminate.

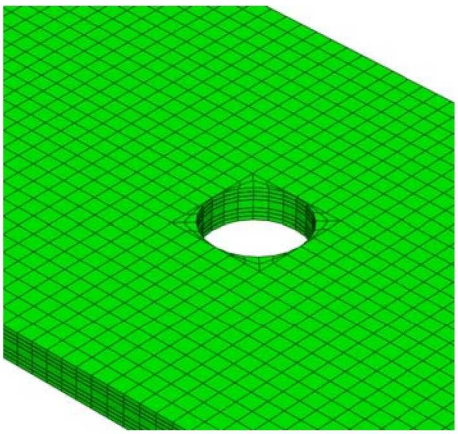

(a) Finite element model.

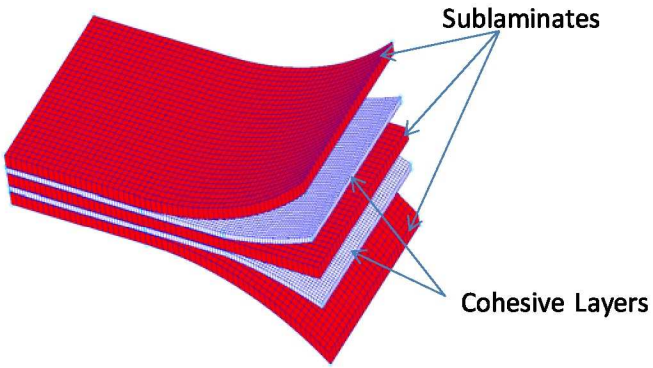

(b) Representation of sub-laminate and cohesive layer modeling.

Figure 3.2. Actual finite element model and the pictorial representation of the sub-laminate and cohesive layers modeling.

The cohesive layers in the 3D model require interfacial properties to simulate delaminations. Hence, the properties including inter-laminar stiffnesses and strengths are evaluated per Equations (3) and (4). In Equation (3) the thickness t was determined based on the number of plies in the sub-laminate

[2] Model configurations include all four lamination stacking sequences provided in Table 3.3 for the 0.5-inch-diameter hole, and only the first three lamination stacking sequences for the 0.25-inch-diameter hole.

sections. The interfacial strengths were calculated by adopting two finite elements in the cohesive zone [32] with the length of the element being 0.02 inches. This modeling practice, to simulate delamination, has provided good results in our previous study [19]; hence, the same practice has been adopted in this study.

The boundary conditions at one end of the specimen were fully clamped (i.e., all three DOFs were constrained) and the boundary conditions at the opposite end of the specimen consisted of two DOFs being constrained (two displacements) with the in-plane longitudinal displacement in the 0° fiber direction being uniformly displaced in the course of the PFA. Each time, the final displacement of 0.070 inches was prescribed over the simulation period of 0.0075 seconds resulting in the displacement loading rate of 9.33 in/s. For a selected group of laminates, two additional final displacement values of 0.040 and 0.055 inches were selected resulting in the reduced displacement loading rates of 5.33 and 7.33 in/s, respectively. The application of alternative displacement loading rates was aimed at assessing the sensitivity of the solution to the displacement loading rates and the applicability of ABAQUS™/Explicit single and double precision solvers. Each time, the displacement loading was applied in a constant-slope ramp fashion.

A mass density of 0.000154 lbs-s^2/in^4 for the composite material was used in the analysis, while the adhesive layer was modeled as being weightless. During the entire simulation, the kinetic energy of the model was monitored to ensure that it did not exceed 10 percent of the total strain energy of the model in accordance with the ABAQUS™ User's Manual guidelines for simulating quasi-static loading in the explicit finite element solver [30]. This guideline (maintaining the kinetic energy to a minimum while simulating a pseudo-static analysis) ensures that significant dynamic effects were not introduced while using a small total loading time required for computational efficiency in an explicit analysis.

3.2 Results and Discussions

In the following sections, results obtained from inter- and intra-laminar PFAs of 8-, 16- and 32-ply-thick laminates with a 0.25-inch- and a 0.5-inch-diameter hole located at the center are presented. The stacking sequences of these laminates are presented in Table 3.3. The results, which include failure stress and the final failure modes exhibited by these laminates, are subsequently presented in tabular and contour plot formats. As outlined in Section 2.1, damages in fiber and matrix in the COSTR model adopt only values of 0 (undamaged) or 1.0 (damaged), and the colors blue and red are used, respectively, to indicate their damage tag status. However, the status of ABAQUS™ cohesive elements changes in a continuous fashion; therefore these plots may also show regions other than blue (not delaminated) and red (completely delaminated), for example green. Elements tagged with colors other than blue or red correspond to the cohesive elements satisfying the inter-laminar failure criteria, but not reaching the complete delamination stage (i.e., still propagating on the degradation part of the traction and separation curve of the cohesive law) [30].

The fractured surface and the failure modes (fiber, matrix and delamination) will be presented for all the laminates. The explanation of failure types [24] exhibited by these laminates from the post failure analysis of the failed specimen will be compared with the failure plots obtained from PFA. The sensitivity of the failure mode and the failure load to loading rate in the 8-ply-thick and 32-ply-thick laminates with a 0.25-inch-diameter hole located centrally will be presented in damage plots and load versus displacement curves.

The experimental data used for the comparison of PFA results is obtained from the work of Green et al. [24]. Depending on the stacking of the same direction plies in a laminate, different failure types

were observed in their experimental study. Final failure types were broadly classified into brittle, pull-out and delamination and are presented in Figure 3.3.

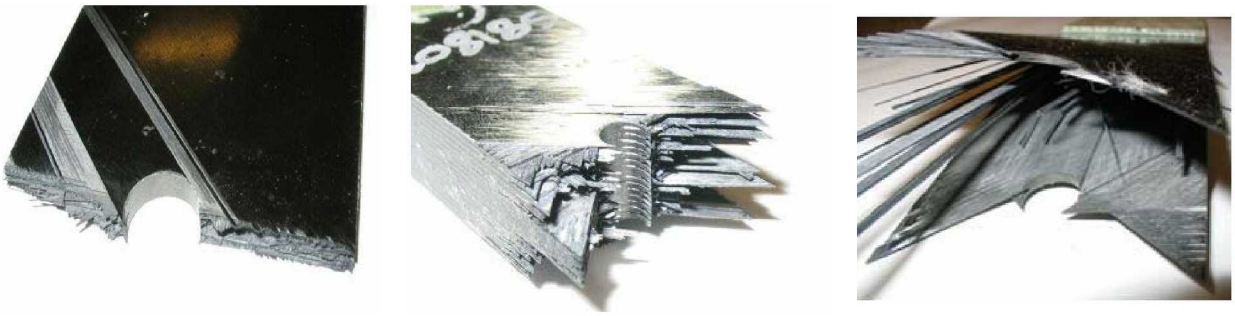

(a) Brittle. (b) Pull-out. (c) Delamination.

Figure 3.3. Final failure types (Ref. 24).

The PFAs of the open-hole tension coupons using the COSTR damage model and the failure methodology presented in the earlier sections were performed on seven laminate configurations. The numerical results (including ultimate failure stress, plots of damage progression, and the load-displacement relationship curves for the 8-, 16-, and 32-ply laminates) along with the experimental results reported in Ref. 24 are presented. Also, the fractured surfaces plots of selected laminates are shown.

3.2.1 0.5-inch-Diameter Hole Specimens

The predictions of failure stress and the final failure type exhibited by the 32-ply sub-laminate-level and ply-level scaled laminates with a 0.5-inch-diameter hole are presented in Table 3.4 and Figures 3.4 through 3.18. The predicted failure stress of the 32-ply ply-level scaled laminates is in good agreement with the available experimental failure stress provided in Table 3.4. The brittle type of failure exhibited by the $[45/90/-45/0]_{4s}$ (sub-laminate-level scaled) laminate, delamination type of failure in the $[45_4/90_4/-45_4/0_4]_s$ (ply-level scaled) laminate, and pull-out type of failure in the $[45_2/90_2/-45_2/0_2]_s$ (ply-level scaled) laminate have all been simulated by the COSTR damage model. The sequence of the occurrence of damage modes in the 32-ply sub-laminate-level and ply-level scaled laminates of the failure process match the experimental observations provided in Ref. 24.

Table 3.4. Test [24] and PFA failure stress results (psi) and damage types of ply-level scaled specimens.

	Number of Plies	8	16	32
0.5-inch-diameter hole	Test	N/A	N/A	52,490
	PFA	63,510	57,130	53,940

Pull-Out Delamination

The load versus end displacement curve of the 32-ply sub-laminate-level scaled specimen is presented in Figure 3.4, where the nearly instantaneous drop to zero past the maximum load value is a reflection of fiber failure in all the plies. Fiber, matrix, and delamination damage modes are presented in Figure 3.5 which demonstrates the characteristics of a brittle failure. The undamaged regions of the specimen are represented in blue and the damaged regions are represented in red. The damage modes in only one of the plies are shown in Figure 3.5 as they are the same in the rest of the neighboring plies with the same alignment. It is clear from Figure 3.5 that the fiber failure occurs in all the plies, and matrix damage and delamination are confined to the crack path only, which is in good agreement with the description provided in Ref. 24 for a brittle type of failure.

Several figures similar to Figure 3.5 are presented in the subsequent portion of the report for different specimen configurations. Readers are cautioned that elements can be tagged as fiber failure as a result of one of the two conditions outlined in section 2.1, i.e., (1) actual fiber failure or (2) an excessive transverse and/or shear strain level. For example, in Figure 3.5, fiber damage in the 90° plies does not occur and the elements are tagged as damaged due to excessive transverse strain levels caused by the matrix damage.

The fractured surface of the 32-ply sub-laminate-level scaled specimen obtained from the PFA and testing are presented in Figure 3.6, showing a clean fracture surface, which is also the characteristic of a brittle type of failure.

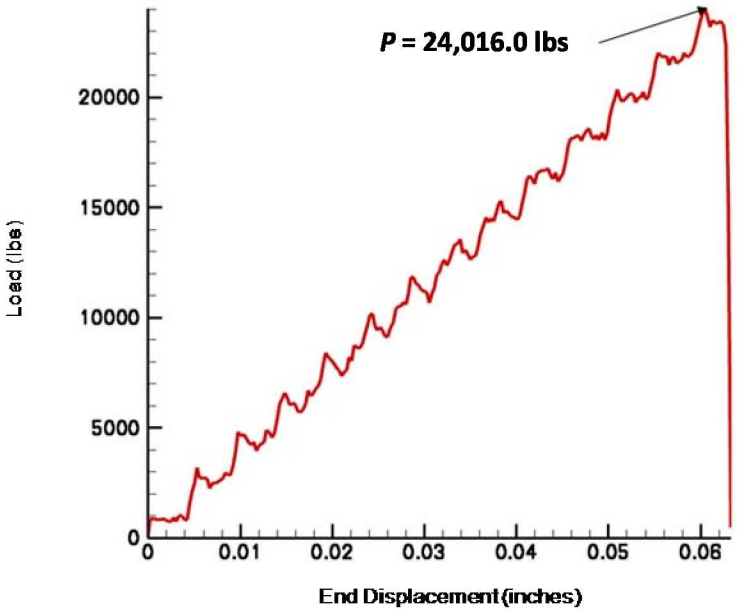

Figure 3.4. Load versus end displacement of a $[45/90/-45/0]_{4s}$ laminate with a 0.5-inch-diameter hole.

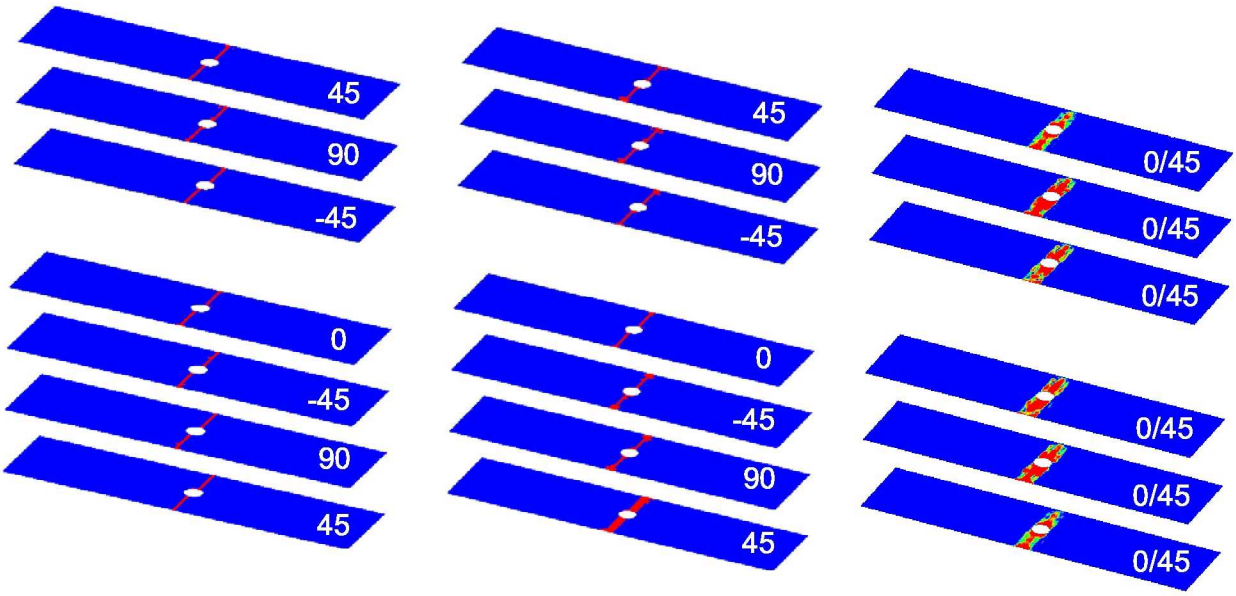

Fiber Failure Matrix Failure Delamination Failure

Figure 3.5. Damaged element tags in a $[45/90/-45/0]_{4s}$ laminate with a 0.5-inch-diameter hole.

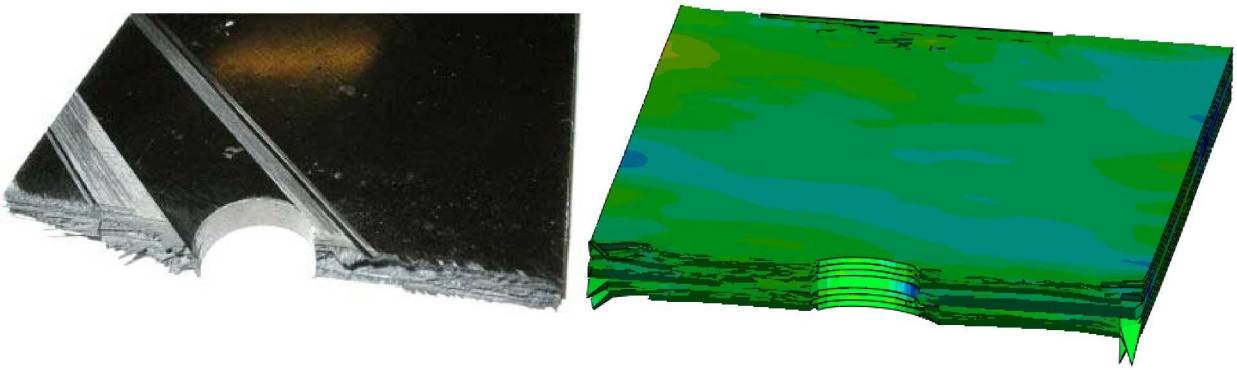

Test Specimen (Ref. 24) Progressive Failure Analysis

Figure 3.6. Crack path in a $[45/90/-45/0]_{4s}$ laminate.

A ply-level scaled $[45_4/90_4/-45_4/0_4]_s$ laminate exhibited a delamination type of failure. According to Green et al. [24], this type of failure exhibits extensive delamination at the –45°/0° interface covering a large portion of the specimen area. This massive delamination triggers a substantial level of load drop due to dissipation of energy. During the delamination process, splitting occurs in the 0° plies and extends over almost the total length of the specimen. This process causes the 0° ply to ultimately fail in the fiber failure mode. This type of failure in the ply-level scaled 32-ply thick specimen was accurately captured by the COSTR damage model. The load versus end displacement plot is shown in Figure 3.7 where the green curve represents the actual data and the red curve is smoothened. Smoothening of the load versus displacement curves in the subsequent portion of the report is applied. As demonstrated in Figure 3.7, the smoothening process averages the load to reduce small oscillations present in the solution due to the loading rate. Usually the test loading rate is extremely low which makes it impractical to perform the explicit analysis using the same loading rate.

The progression of the damage modes is presented in Figures 3.8 through 3.11. The damage state at the maximum load of 22,811.7 lbs is shown in Figure 3.8, which corresponds to point A in Figure 3.7. Point A is just before the occurrence of massive delamination, however no fiber failure was detected in any of the plies at this point of loading. Only very limited matrix damage and delaminations around the hole are present. The damage state at a load level of 22,223 lbs, corresponding to point B in Figure 3.7, is shown in Figure 3.9 where the splitting (matrix damage) in the 0° ply and the propagation of delamination at the –45°/0° interface is presented as both of these damages further develop. The damage state at a load level of 18,721 lbs is shown in Figure 3.10 where the propagation of delamination at the –45°/0° interface, splitting in 0° plies, and substantial matrix damages in off-axis plies are shown even as the load reduces to a level corresponding to point C in Figure 3.7. The damage state at a load level of 13,039 lbs is shown in Figure 3.11 where the complete delamination at the –45°/0° interface and also, to a significant level, at other interfaces with splitting in 0° plies reaching the very end of grips are predicted. The damage state shown in Figure 3.11 corresponds to point D in Figure 3.7 at which point the analysis was terminated. This phenomenon of splitting in the 0° plies, which causes discontinuity in the axial deformation, is captured and presented in Figure 3.12. The other significant characteristic of delamination type of failure is the absence of fiber failure in the 0° plies during the loading cycle. The fiber failure simulation in the plies is shown in Figure 3.13 (a) and demonstrates that fibers in the 0° plies have not failed even as the load drops significantly to a level corresponding to point D in Figure 3.7. Fiber damage tags around the hole in the 0° plies, as well as the ±45° plies, are due to the failure of elements in matrix mode caused by the excessive transverse and/or shear strains. Tagging these elements as fiber failure facilitates their removal from the analysis to avoid numerical convergence issues associated with severely distorted elements. The process of removing elements also helps in simulating crack paths and can be noticed in the severely disintegrated laminate shown in Figure 3.13 (b).

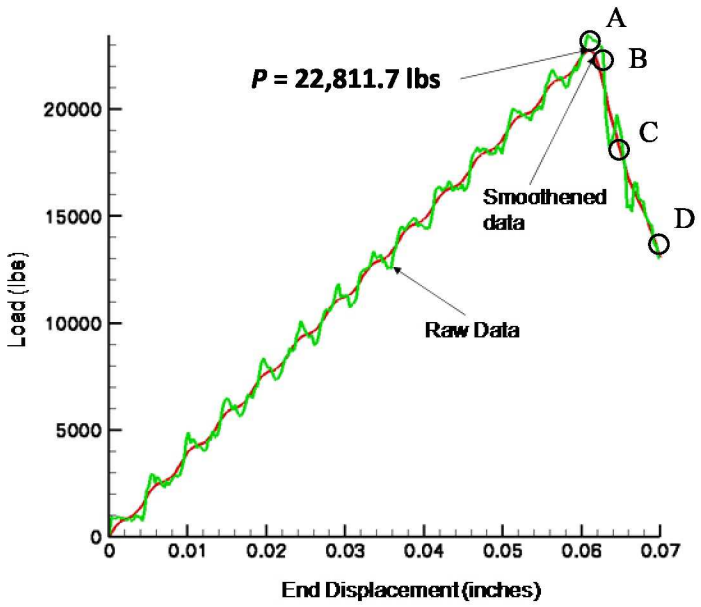

Figure 3.7. Load versus end displacement of a $[45_4/90_4/-45_4/0_4]_s$ laminate with a 0.5-inch-diameter hole.

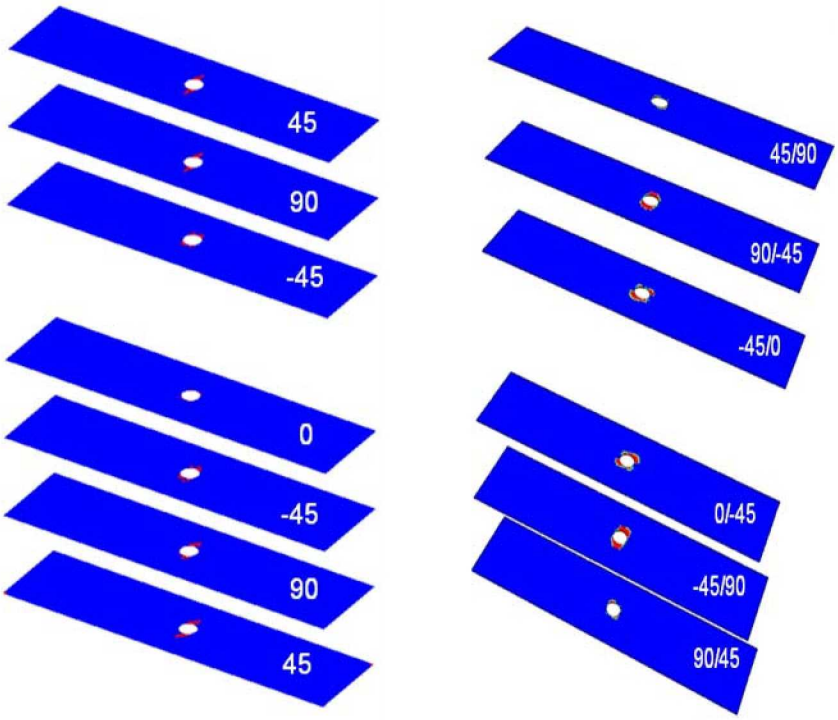

Fiber Failure Delamination Failure

Figure 3.8. Damaged element tags in a $[45_4/90_4/-45_4/0_4]_s$ laminate with a 0.5-inch-diameter hole at P = 22,811 lbs (point A in Figure 3.7).

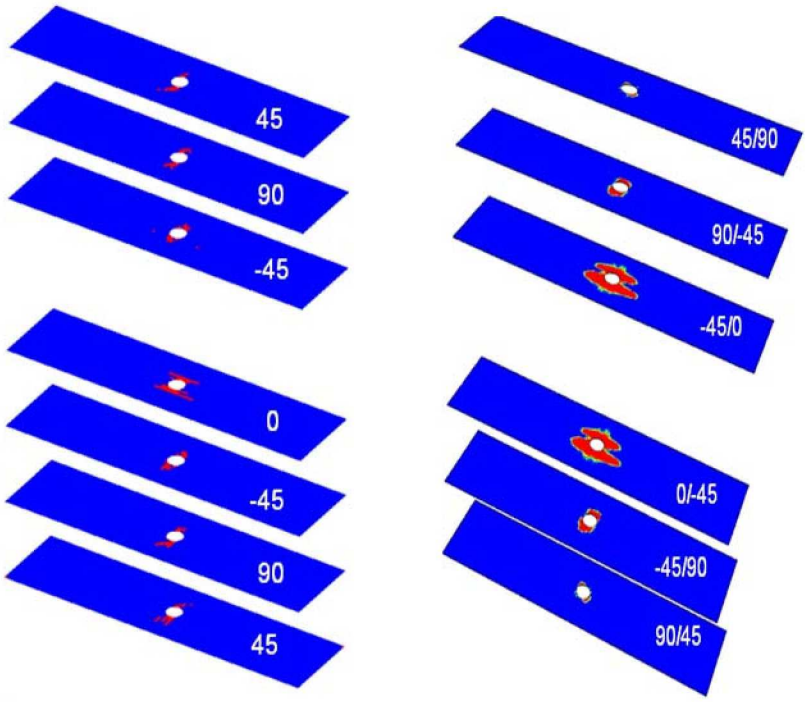

Fiber Failure Delamination Failure

Figure 3.9. Damaged element tags in a $[45_4/90_4/-45_4/0_4]_s$ laminate with a 0.5-inch-diameter hole at P = 22,223 lbs (point B in Figure 3.7).

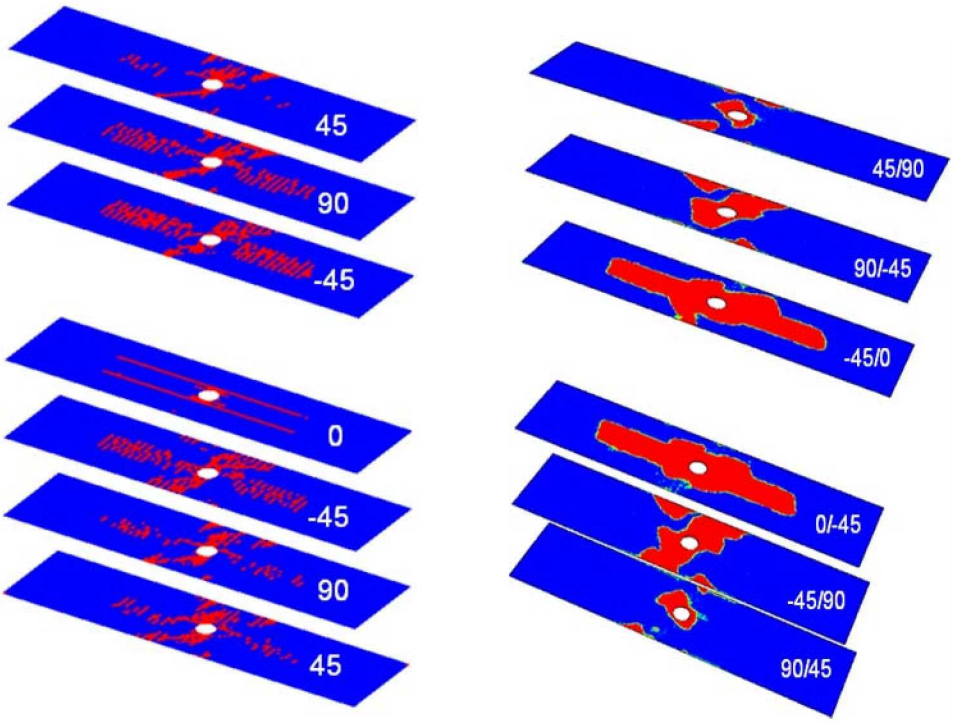

Fiber Failure Delamination Failure

Figure 3.10. Damaged element tags in a $[45_4/90_4/-45_4/0_4]_s$ laminate with a 0.5-inch-diameter hole at P = 18,721 lbs (point C in Figure 3.7).

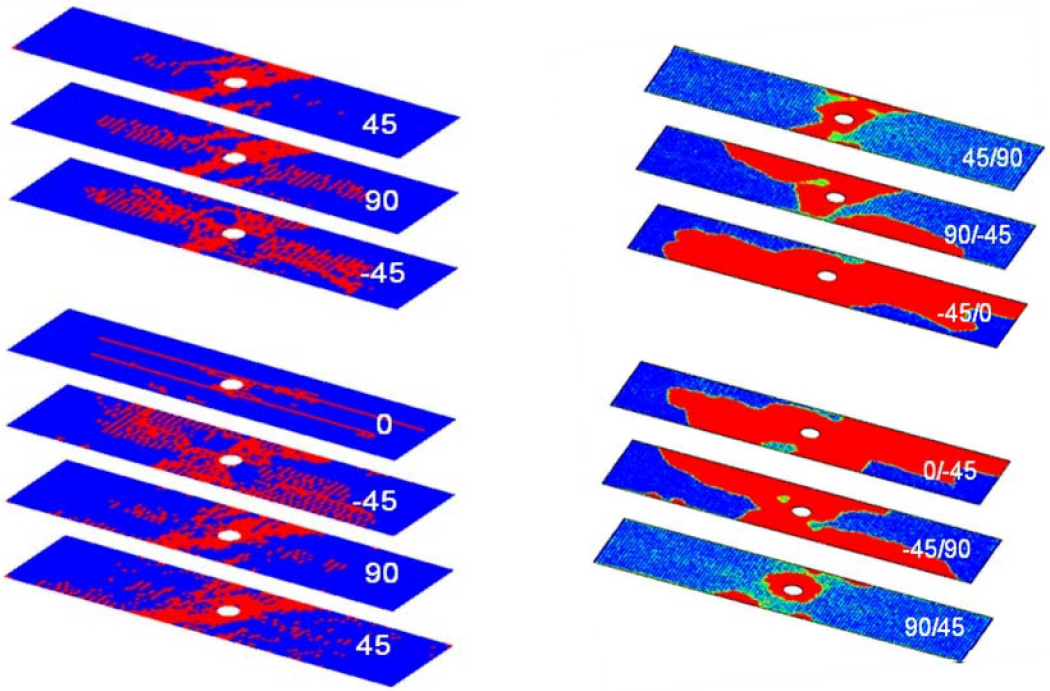

Fiber Failure Delamination Failure

Figure 3.11. Damaged element tags in a $[45_4/90_4/-45_4/0_4]_s$ laminate with a 0.5-inch-diameter hole at P = 13,039 lbs (point D in Figure 3.7).

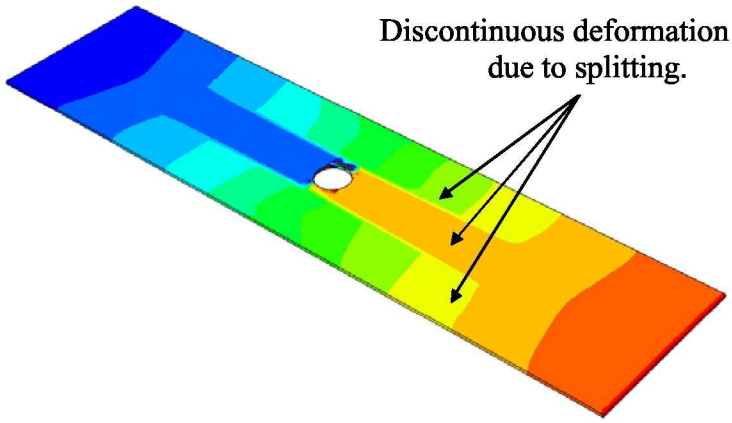

Figure 3.12. Axial deformation in the 0° plies due to splitting.

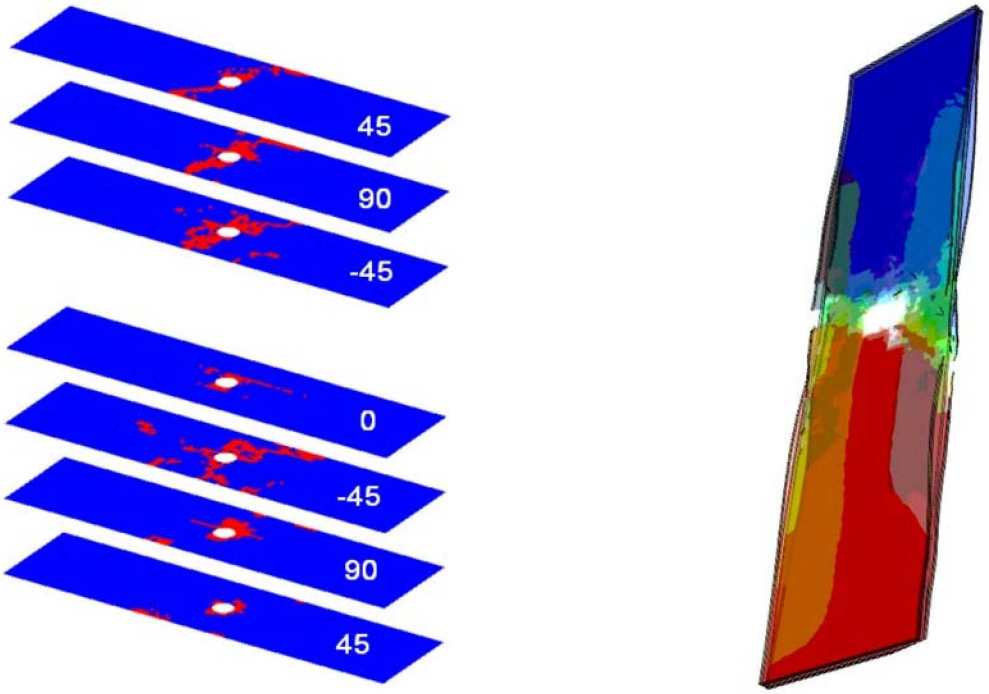

(a) Damaged element tags. (b) Delamination failure.

Figure 3.13. $[45_4/90_4/-45_4/0_4]_s$ laminate with a 0.5-inch-diameter hole at $P = 13{,}039$ lbs.

The PFA of a 16-ply $[45_2/90_2/-45_2/0_2]_s$ laminate predicted a pull-out type of failure. The pull-out failure, as defined in Ref. 24, can be described as failure in which the fibers in the 0° plies fail and their failure is accompanied by delamination at the –45°/0° interface and at the other interfaces of the off-axis plies. The load versus end displacement curve with a sudden drop, as presented in Figure 3.14, indicates the 0° plies fiber failure. The PFA was terminated after fiber failure occurred in the 0° plies. The crack path in the 0° plies which represents fiber failure is shown in Figure 3.15. The damage modes associated

with this type of failure are presented in Figure 3.16. There is little to no fiber failure in the off-axis plies except in the 0° and 90° plies. The matrix damage occurs in all the plies and the extent of this damage is limited to approximately two times the distance between the hole and the specimen edge. A complete delamination across the full width of the specimen with longitudinal extension of approximately double the specimen width was noticed in the –45°/0° interfaces around the hole. However, the delamination at the other interfaces was discontinuous in some regions.

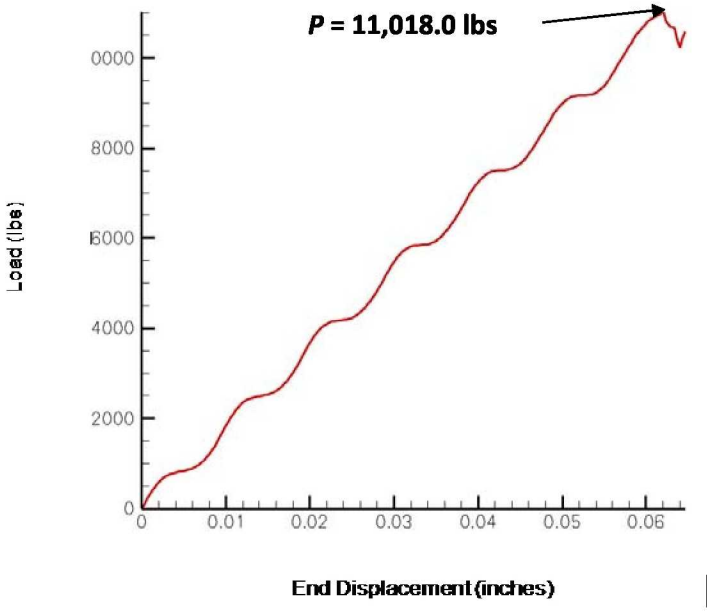

Figure 3.14. Load versus end displacement of a $[45_2/90_2/-45_2/0_2]_s$ laminate with a 0.5-inch-diameter hole (curve smoothened).

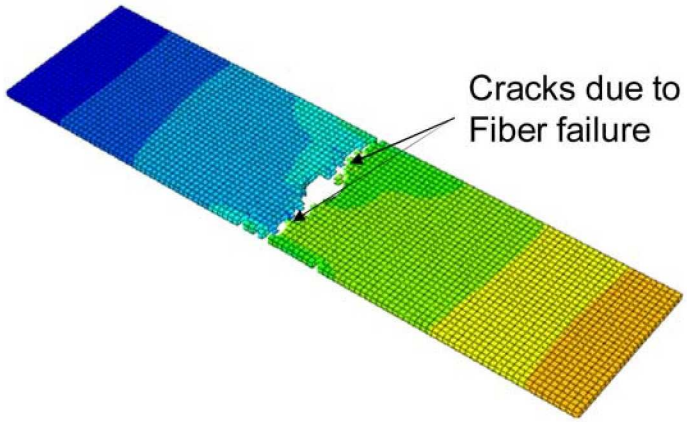

Figure 3.15. Crack path in the 0° plies of a $[45_2/90_2/-45_2/0_2]_s$ laminate with a 0.5-inch-diameter hole past the maximum load of P = 11,018 lbs.

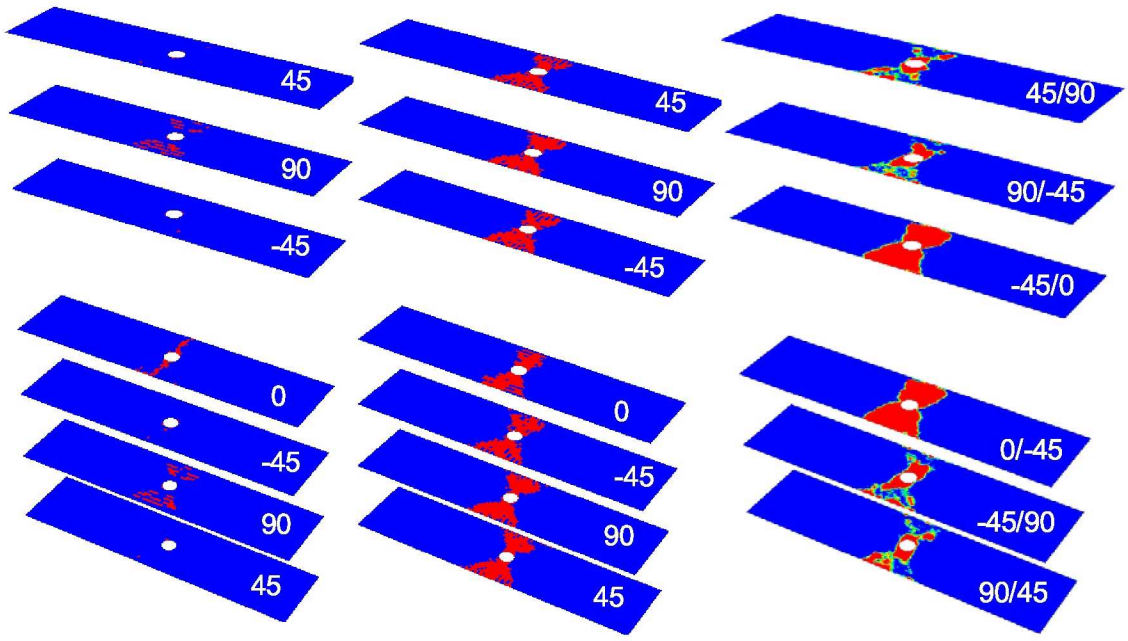

Fiber Failure Matrix Failure Delamination Failure

Figure 3.16. Damaged element tags in a $[45_2/90_2/-45_2/0_2]_s$ laminate with a 0.5-inch-diameter hole past the maximum load of $P = 11{,}018$ lbs.

The same pull-out type of failure was predicted in the 8-ply $[45/90/-45/0]_s$ laminate with a 0.5-inch-diameter hole. The damage plots presented in Figure 3.17 reveal the type of damage modes characteristic to the pull-out type failure. The curve presented in Figure 3.18 also shows an instantaneous loss in load-carrying capability in the specimen due to fiber failure in the load-carrying 0° plies.

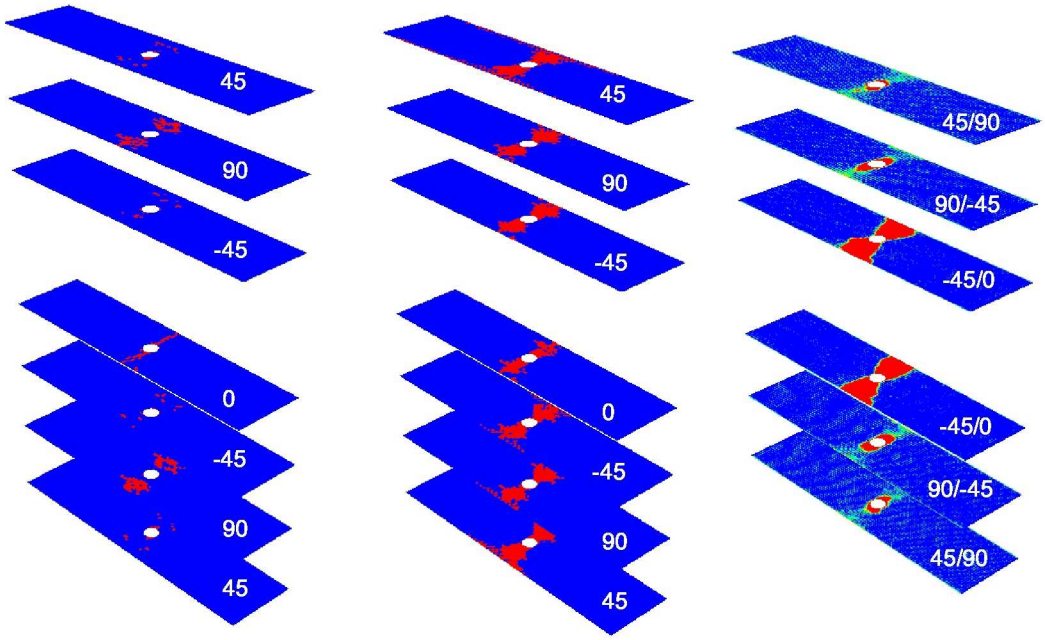

Fiber Failure Matrix Failure Delamination Failure

Figure 3.17. Damaged element tags in a $[45/90/-45/0]_s$ laminate with a 0.5-inch-diameter hole.

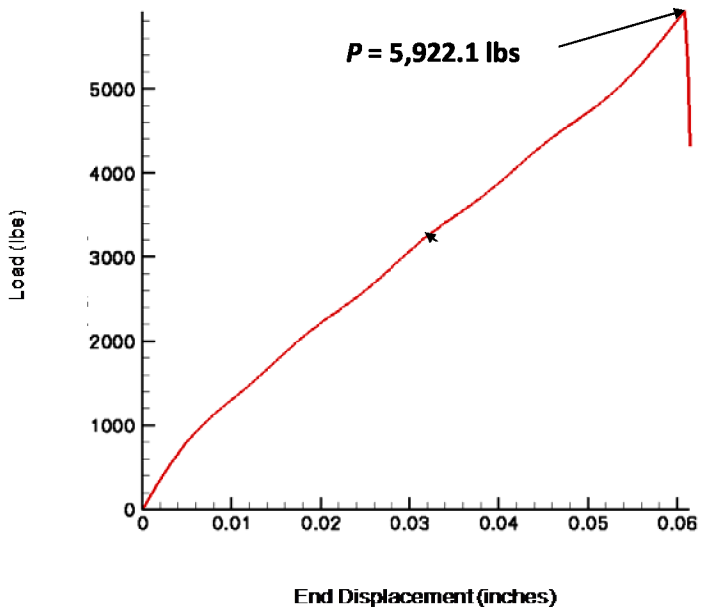

Figure 3.18. Load versus end displacement of a $[45/90/-45/0]_s$ laminate with a 0.5-inch-diameter hole (curve smoothened).

3.2.2 0.25-inch-Diameter Hole Specimens

The results obtained from the PFA for the specimens with a 0.25-inch-diameter central hole are presented in Table 3.5 and Figures 3.19 through 3.26. The failure stresses of the 8-, 16-, and 32-ply laminates presented in Table 3.5 are in good agreement with the test results where the latter are available in Ref. 24. The average percentage difference in ultimate failure stress between the experimental data and the PFA results for the 16- and 32-ply laminates are 6.4 percent and 5.1 percent, respectively.

Table 3.5. Test [24] and PFA failure stress results (psi) and damage types in ply-level-scaled specimens.

	Number of Plies	8	16	32
0.25-inch-diameter hole	Test	N/A	72,210	56,550
	PFA	64,300	67,570	59,595

Brittle | Pull-Out | Delamination

The failure type predictions for the 16- and 32-ply laminates are similar to the 0.5-inch-diameter hole specimens and are in good agreement with the experimental observations made by the authors in Ref. 24. A delamination type of failure was simulated for the 32-ply laminate and the same was observed in the test. In this case, the load drop due to delaminations as observed in the load versus end displacement curve presented in Figure 3.19, was small when compared with the load drop in the 0.5-inch-diameter hole coupon with the same laminate configuration. The ultimate failure load value of 12,366 lbs is shown in Figure 3.19 and is slightly greater than the load at which the delamination occurred. The propagation of damage modes in terms of fiber, matrix, and delamination failures in this laminate are presented in Figures 3.20 through 3.24. The damage state at the loads of 12,148 lbs, 11,905 lbs and 12,366 lbs are shown in Figures 3.20 through 3.22 corresponding to points A, B and C in Figure 3.19, respectively. The subcritical damages around the hole before the occurrence of major splitting can be noticed. Figure 3.21 illustrates how the evolution of splitting (matrix damage) in the 0° plies, as well as the matrix damage in off-axis plies, causes delamination to grow in the –45°/0° interfaces. However, no fiber damage in any of the plies is seen at this load level. As the splitting in the 0° plies extends and approach the grip ends, massive delaminations covering almost the entire length of the coupon in the –45°/0° interface and significant delaminations at other interfaces can be observed (see Figure 3.22). The splitting in the 0° plies can be noticed in Figure 3.23 and was captured just past the peak loading shown in Figure 3.19. Complete disintegration of the specimen with fiber failure in the 0° plies and extensive matrix failure in all the plies can be noticed in Figure 3.24, where the next step in damage progression is shown.

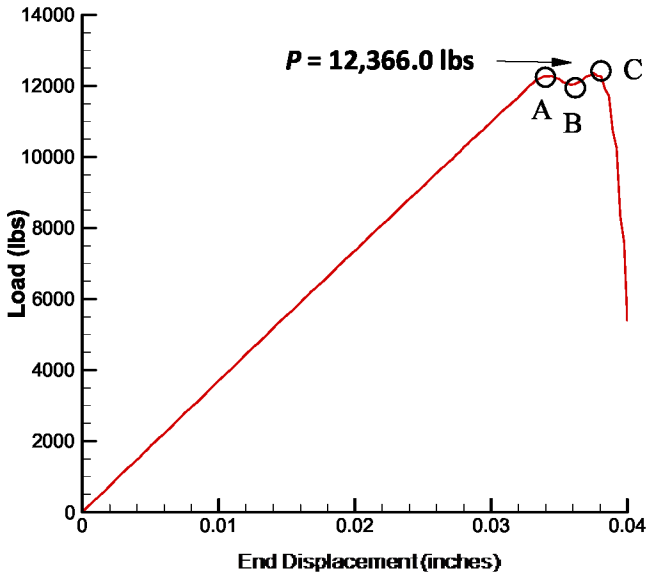

Figure 3.19. Load versus end displacement of a $[45_4/90_4/-45_4/0_4]_s$ laminate with a 0.25-inch-diameter hole (curve smoothened).

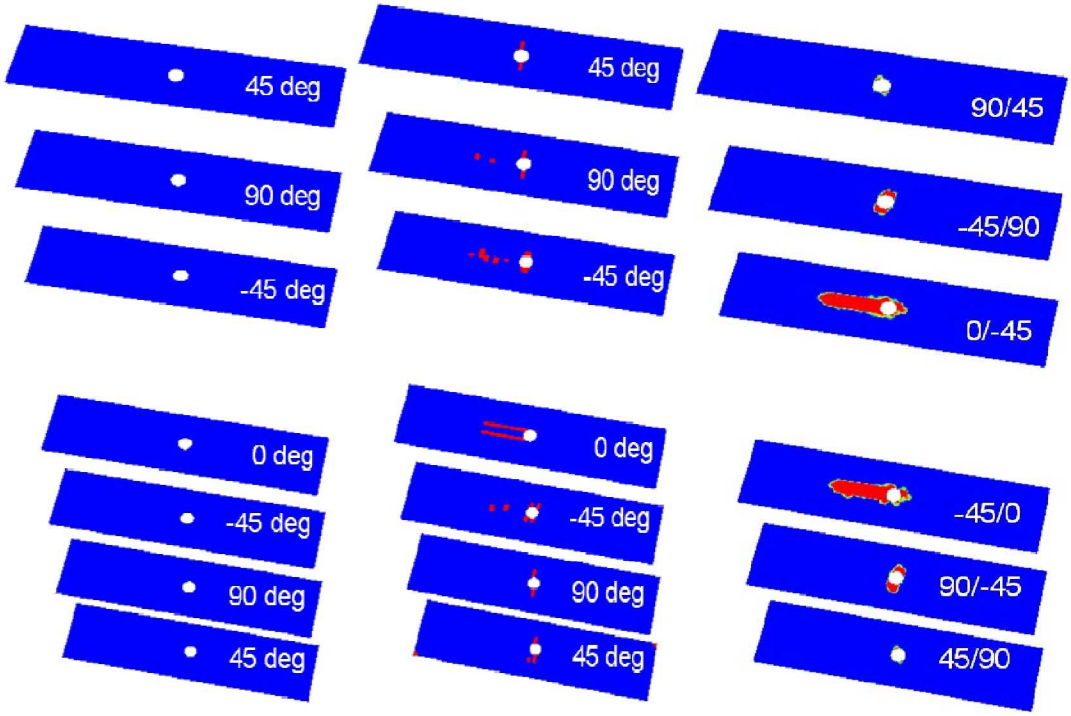

Figure 3.20. Damaged element tags in a $[45_4/90_4/-45_4/0_4]_s$ laminate with a 0.25-inch-diameter hole at $P = 12{,}148$ lbs.

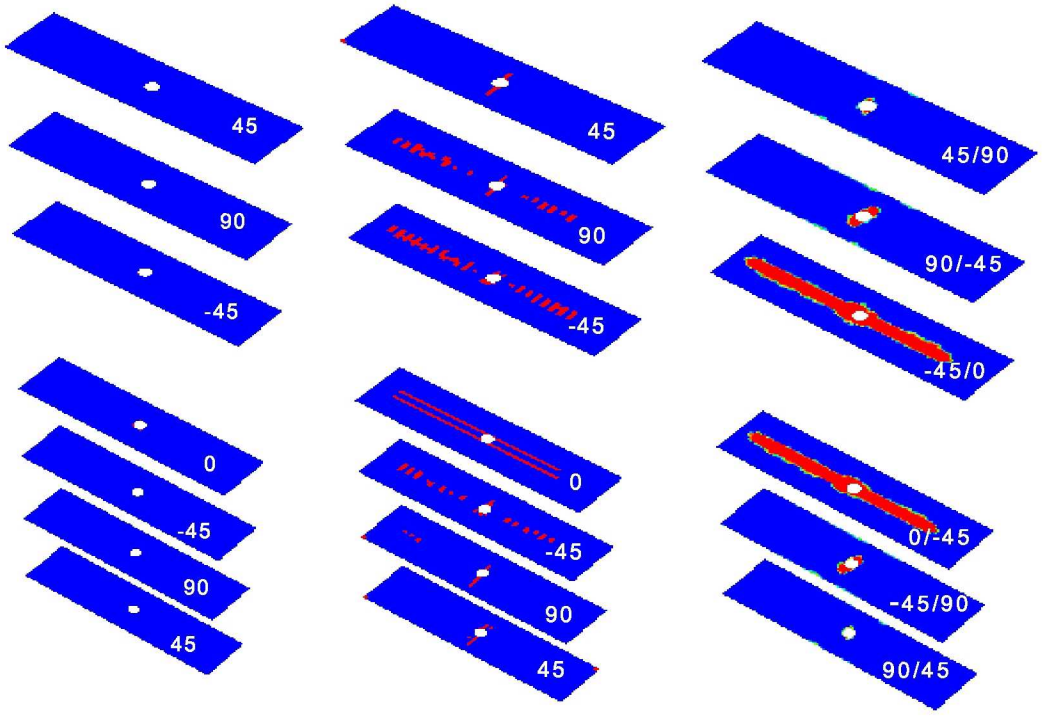

Figure 3.21. Damaged element tags in a $[45_4/90_4/-45_4/0_4]_s$ laminate with a 0.25-inch-diameter hole at $P = 11{,}905$ lbs.

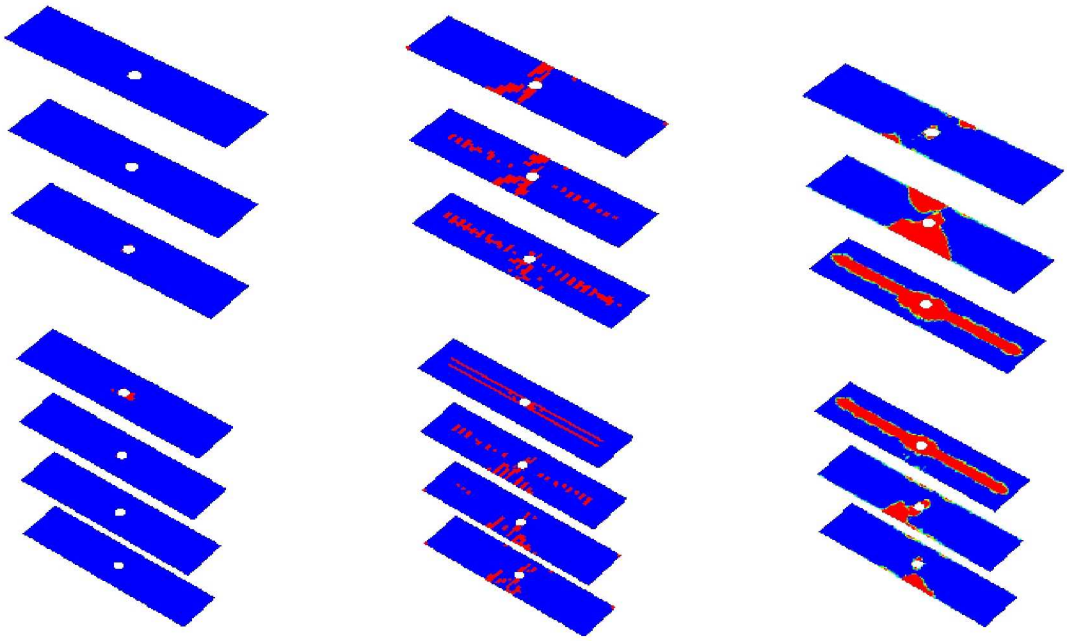

Figure 3.22. Damaged element tags in a $[45_4/90_4/-45_4/0_4]_s$ laminate with a 0.25-inch-diameter hole at $P = 12{,}366$ lbs.

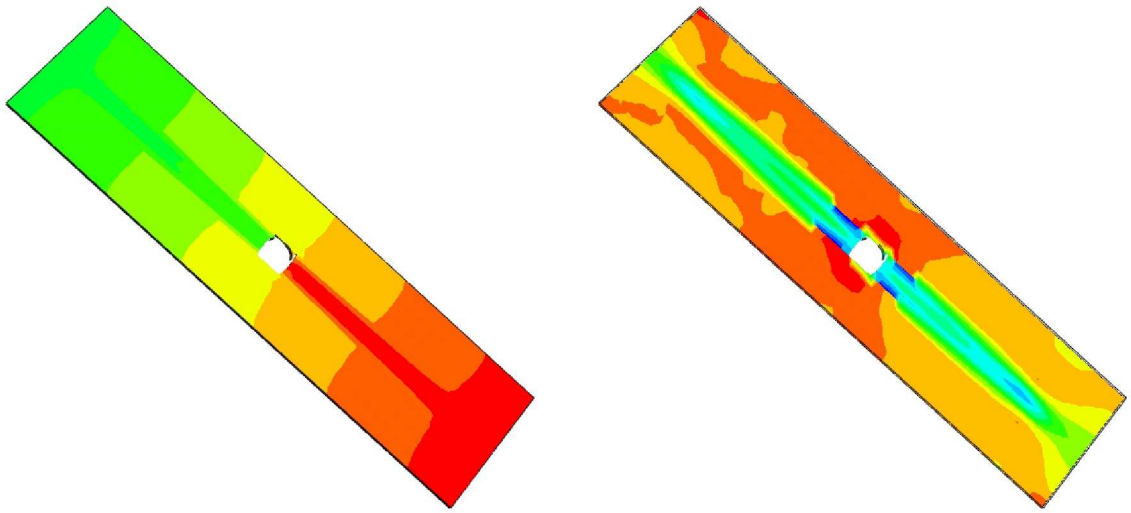

Figure 3.23. Axial deformation and stress field in the 0° plies of a $[45_4/90_4/-45_4/0_4]_s$ laminate with a 0.25-inch-diameter hole due to splitting.

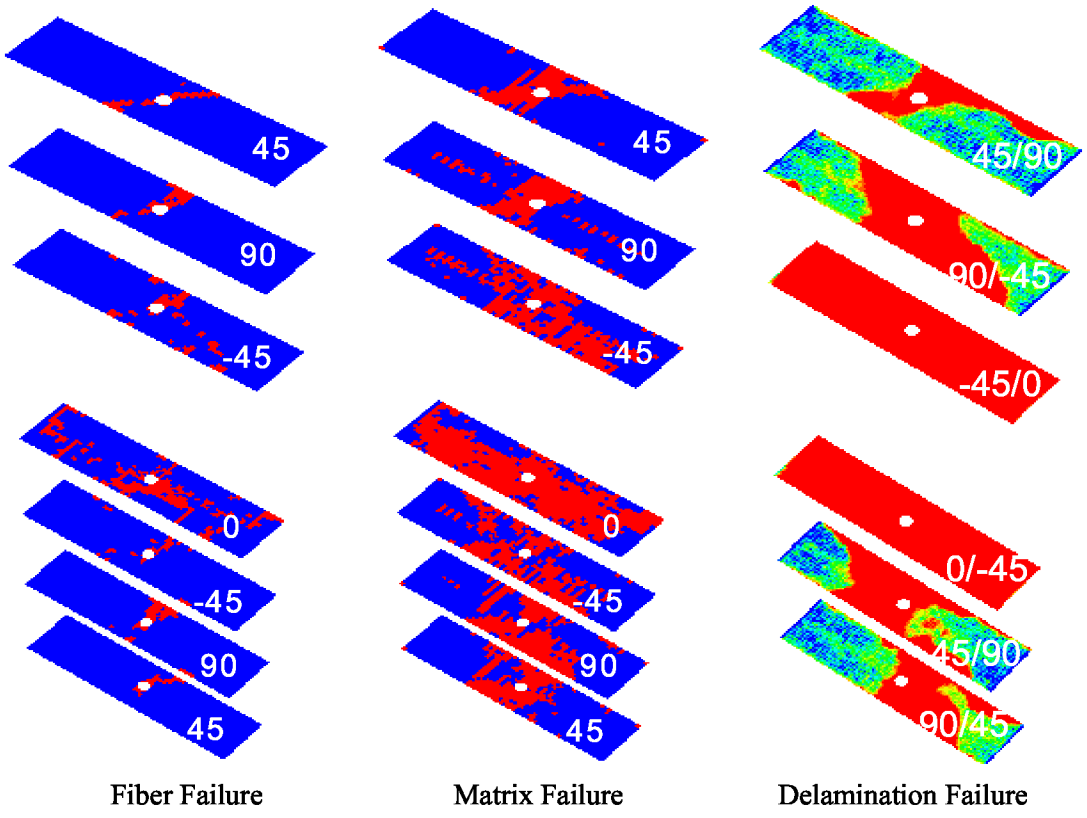

Figure 3.24. Damaged element tags in a $[45_4/90_4/-45_4/0_4]_s$ laminate with a 0.25-inch-diameter hole after catastrophic failure.

The damage modes and the failure types obtained from the PFA of a 16-ply laminate are very similar to those obtained for the specimen with a 0.5-inch-diameter hole. The laminate failed in a pull-out failure type where the 0° plies failed in fiber failure mode. This failure type is indicated by an instantaneous load reduction to zero in the load versus end displacement curve presented in Figure 3.25. Due to this fiber failure, delamination occurs in the –45°/0° interface and also is propagated to the other interfaces. The corresponding damage modes are presented in Figure 3.26. Some fiber failure is noticed in the ±45° and 90° plies, but the failure occurs predominantly in the matrix failure mode. The delamination in the –45°/0° interface extends across the full width of the specimen, but other interfaces also show patchy and discontinued delamination regions. Similar damage modes and damage types were also observed by Green et al. [24] in their experiment.

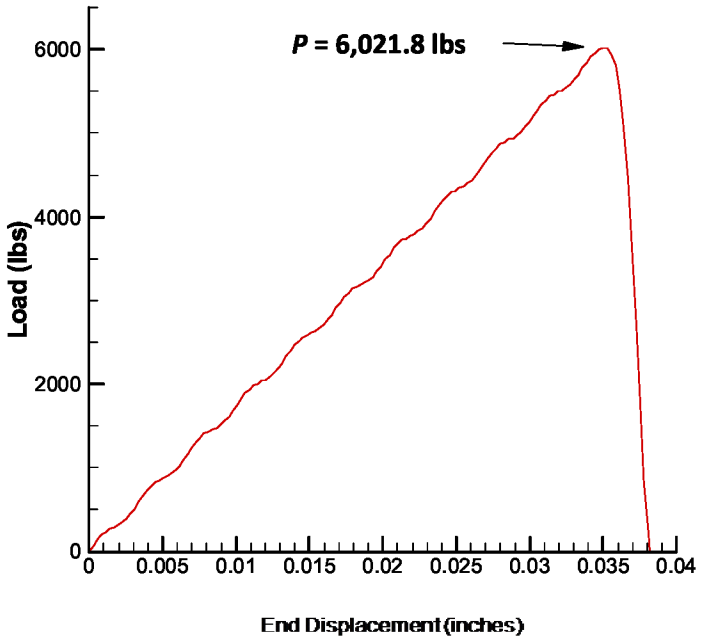

Figure 3.25. Load versus end displacement of a $[45_2/90_2/-45_2/0_2]_s$ laminate with a 0.25-inch-diameter hole (curve smoothened).

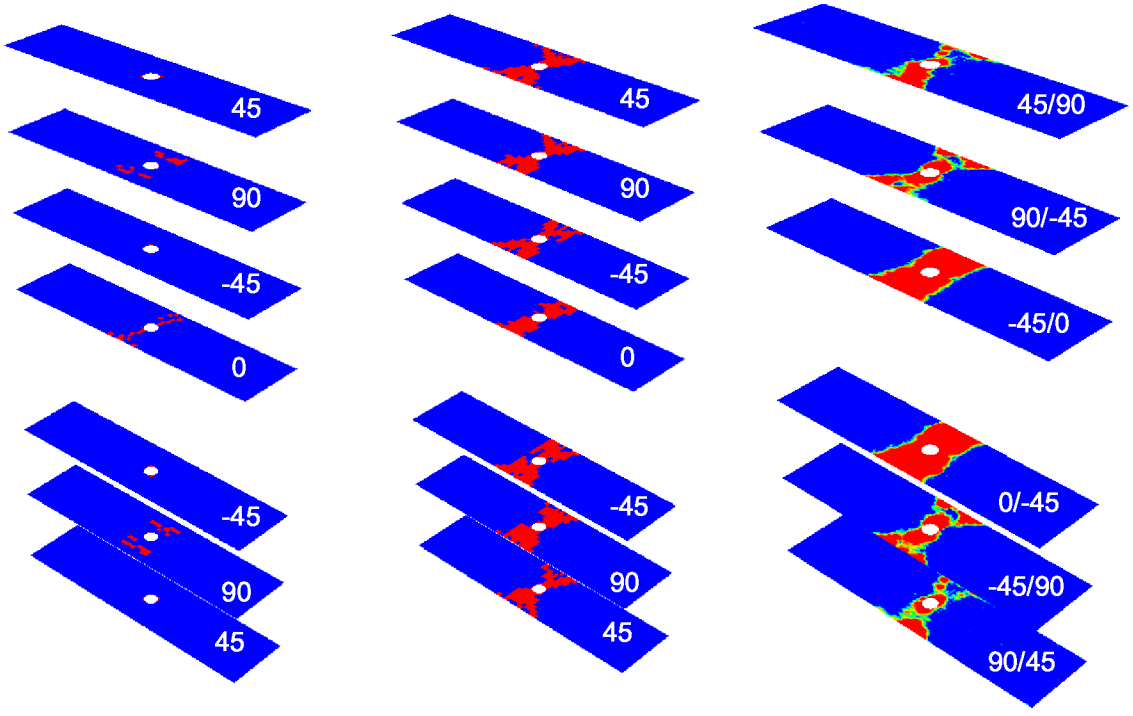

Figure 3.26. Damaged element tags in a $[45_2/90_2/-45_2/0_2]_s$ laminate with a 0.25-inch-diameter hole after catastrophic failure.

PFA of an 8-ply laminate indicates a brittle type of failure. The load versus end displacement curve presented in Figure 3.27 indicates an instantaneous reduction in the load-carrying capability of the

structure, which is an indication of fiber failure in the 0° plies. This type of behavior in the load versus end displacement curve is very similar to the pull-out type failure, but the fiber failure in this laminate differs. Fiber failure is present in all the plies except the 90° plies (because the loading and the fiber direction are perpendicular to each other) as shown in Figure 3.28. The matrix failure is also observed in all the plies. A continuous delamination across the full width of the specimen is present in the –45°/0° interface, but patchy and discontinuous delaminations are present in all other interfaces. The important feature distinguishing the failure type from the pull-out and brittle failures is the failure of fibers in all the plies. This behavior is very well captured as presented in Figure 3.28.

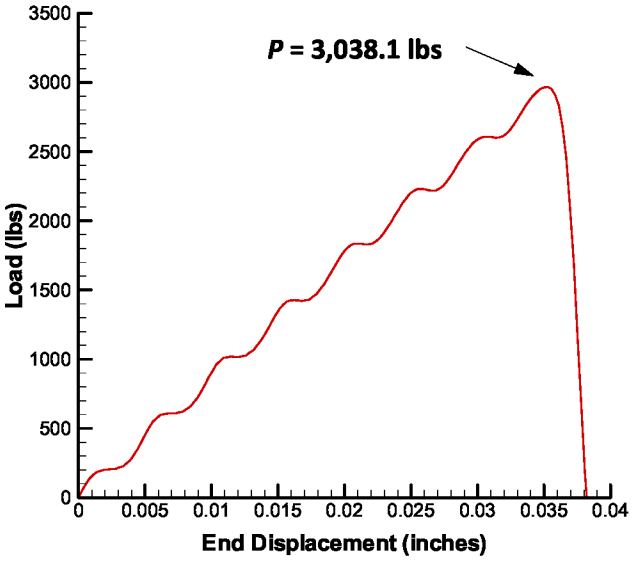

Figure 3.27. Load versus end displacement of a $[45/90/-45/0]_s$ laminate with 0.25-inch-diameter hole (curves smoothened).

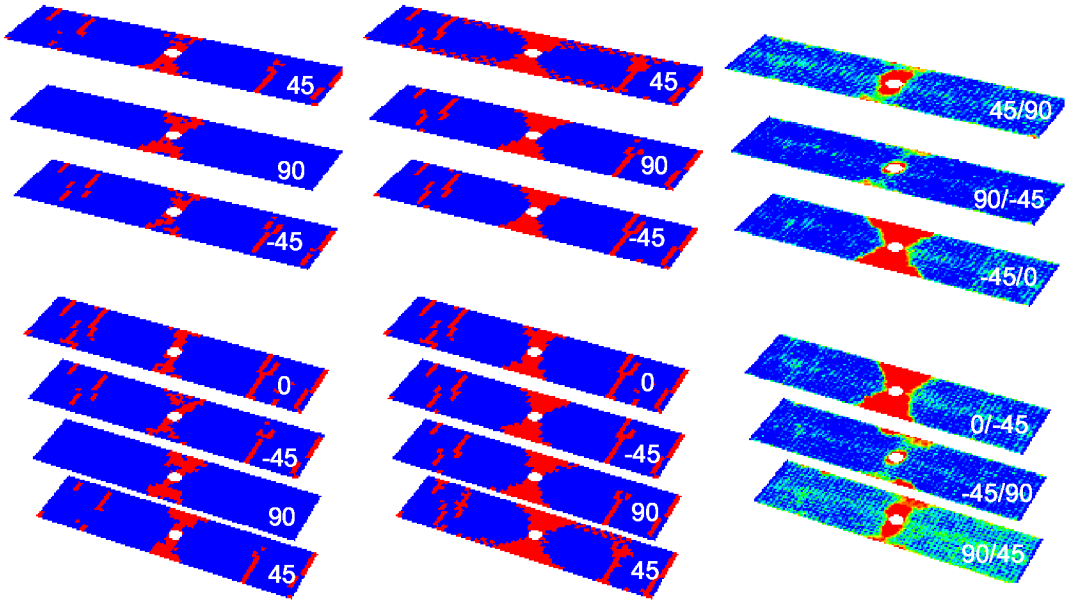

Fiber Failure Matrix Failure Delamination Failure

Figure 3.28. Damaged element tags in a $[45/90/-45/0]_s$ laminate with 0.25-inch-diameter hole after catastrophic failure.

3.2.3 *Sensitivity of Damage Mode and Failure Type to Single and Double Precision Explicit Runs; Capturing Sub-Critical Damages*

As indicated before, the PFA presented herein has been performed using ABAQUS™/Explicit solver. The explicit transient dynamic nonlinear analysis is very efficient in solving problems involving material degradation and simulation of dynamic crack paths. In general, the explicit transient dynamic procedure requires small time increments which depend on the highest natural frequency of the model and are independent of the type and duration of loading. An explicit method can take approximately 10,000 to 1,000,000 increments to complete an analysis run depending on the duration of loading [30]. Solving a problem with a quasi-static loading condition in the actual time scale using explicit solver could require an extremely high number of time steps. To accelerate the solution, the analysis loading rate can be increased, but the kinetic energy in the structure under analysis must be kept at an insignificant level. Due to accumulation of round-off errors occuring while analyzing problems that require more than 300,000 iterations, ABAQUS™ recommends using double precision explicit solver regardless of the loading rate. Hence, a sensitivity study was performed to understand the influence of round-off errors on damage modes and failure types in the 8- and 32-ply laminates with a 0.25-inch-diameter hole.

In this study, end displacements of 0.040, 0.055, and 0.070 inches were applied to the 32-ply laminate over the same analysis period of 0.0075 seconds, resulting in the loading rates of 5.33, 7.33, and 9.33 in/s, respectively. All the above-mentioned cases were analyzed using single precision runs. Additionally, a double precision run was performed for the case with end displacement of 0.04 inches (i.e., the case for which the loading rate was the slowest and, consequently, required the highest number of time integration increments).

For the 8-ply laminate, end displacements of 0.04 and 0.07 inches were applied in 0.0075 seconds, resulting in the loading rates of 5.33 and 9.33 in/s. Both analyses were performed with the single precision solver.

The precision, load rate, number of iterations and damage type obtained from these analyses have been tabulated in Table 3.6. For the 32-ply laminate, the single precision run and the double precision run predicted different failure types when the 0.04-inch end displacement was applied. Note that these two cases required significantly more than 300,000 iterations to complete the analyses due to the slowest loading rate of 5.33 in/s being applied. However, the failure types predicted with the two remaining faster loading rates of 7.33 and 9.33 in/s were the same and consistent with the previously described double precision run. At the same time, the two single precision runs with 0.055- and 0.070-inch end displacements required only around 300,000 iterations or less. A pattern consistent with the data from Table 3.6 can also be noticed based on the load versus end displacement curves presented in Figure 3.29. It is observed that the 0.04-inch end displacement case analyzed with the single precision solver shows instantaneous failure consistent with the pull-out damage. However, the remaining three curves show lower levels of load drop consistent with the delamination damage. The fact that the ultimate failure load in this case is similar for all four analyses attests to the fact that there coexists two competing failure types, and that a small perturbation in the solution procedure can trigger the onset of one of the two distinct damage types. Consequently, further investigation revealed that the shear and axial stresses in the 0° plies of the 32-ply laminate were approaching the failure limit almost at the same time. Such coexistence of damage modes was also documented in experimental work by Green et al. [24]. Nevertheless, based on the ABAQUS™ documentation guidelines pertaining to the applicability of the single precision solvers, the solution obtained with the 0.04-inch end displacement and the single precision solver must be deemed unreliable.

Table 3.6. Failure type and number of iterations to perform PFA for a 0.25-inch-diameter hole laminate.

Laminate	Loading Rate (in/s)	ABAQUS™/Explicit Solver Precision	Number of Iterations	Damage Type
32-ply	5.33	Single	344,289	Pull-Out
	7.33	Single	304,324	Delamination
	9.33	Single	211,839	Delamination
	5.33	Double	346,859	Delamination
8-ply	5.33	Single	367,500	Pull-Out
	9.33	Single	212,062	Pull-Out

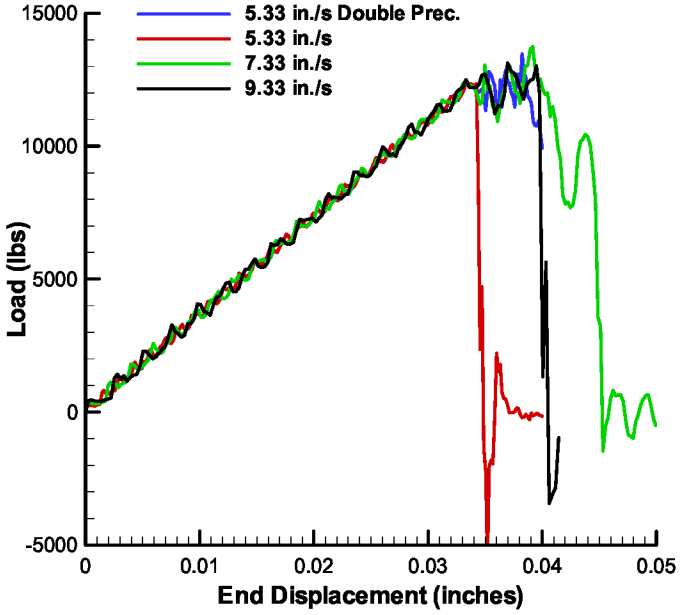

Figure 3.29. Load versus end displacement of a $[45_4/90_4/-45_4/0_4]_s$ laminate with a 0.25-inch-diameter hole (curves smoothened).

The prediction of sub-critical damages in the form of splitting (matrix damage parallel to fibers) within the plies, and the delaminations between the plies using the COSTR damage model and the modeling procedure explained in earlier sections are presented in Figure 3.30 and Figure 3.31 for a 32-ply-thick ply-level scaled laminate with a 0.5-inch-diameter hole at the center. The integrated sub-critical damages of all the plies are shown in these figures; and hence, the color of the damage in the top ply appears brightest and gradually fades as the damage reaches the bottom most ply. Analyzing Figure 3.30 and Figure 3.31 one can see that the sub-critical damage between the plies (delamination) has been predicted well for 80 percent and 95 percent of the load level. However, the predictions of sub-critical damages within the plies (splitting) have been predicted qualitatively. The modeling parameters such as the mesh size and the mesh shapes used in the current analyses are not conclusive in predicting these micro cracks (splitting) quantitatively. These sub-critical damages seem to be qualitatively similar for all laminate sizes analyzed here, even though the failure types and the failure stress are different. Similar observations were also made by authors in Ref. 24.

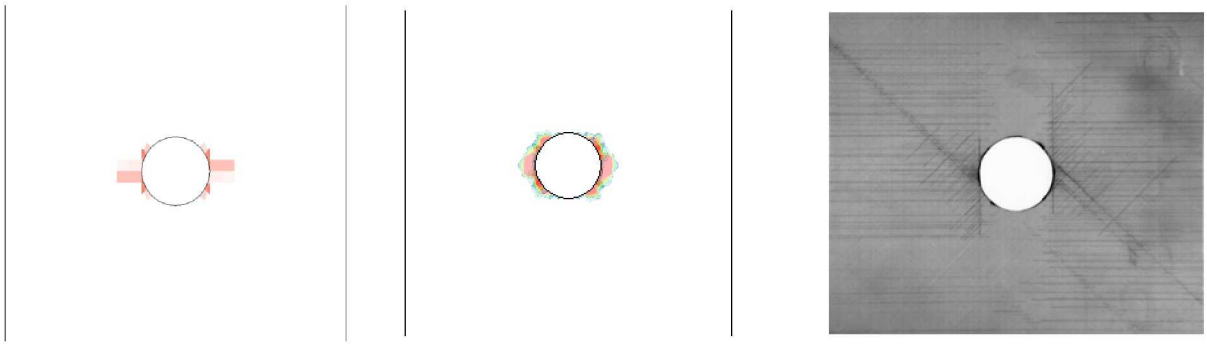

(a) Splitting. (b) Delamination predictions. (c) X-ray image of damage.

Figure 3.30. PFA for a $[45_4/90_4/-45_4/0_4]_s$ laminate with a 0.5-inch-diameter hole loaded to 80 percent of failure load (Ref. 24).

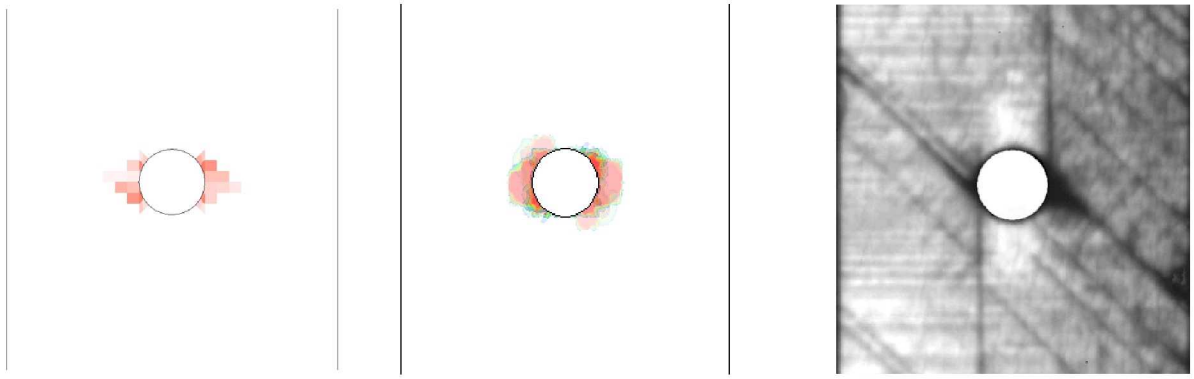

(a) Splitting. (b) Delamination predictions. (c) X-ray image of damage.

Figure 3.31. PFA for a $[45_4/90_4/-45_4/0_4]_s$ laminate with a 0.5-inch-diameter hole loaded to 95 percent of failure load (Ref. 24).

Additional damage plots obtained with both single and double precision solvers, and corresponding to several different loading levels, and are presented in Figures 3.32 through 3.42, where sub-plots (designated by (a)) present the corresponding point on the load-displacement curve, and the subsequent sub-plots present the fiber, matrix and/or delamination damage tags. These figures provide not only a more detailed insight into sensitivity of damage mode and type to single and double precision explicit runs, but also show how sub-critical damages are developed when the COSTR damage model is applied.

It is seen that for the most part the load application (i.e., between the end displacement of 0.0024 inches (Figure 3.32) and the end displacement of 0.0306 inches (Figure 3.38)), the sub-critical damages obtained from both solvers are nearly identical. The first delamination is already identified at a very small end displacement of 0.0024 inches in the –45°/0° interfaces as presented in Figure 3.32 (b) and (c). A delamination in the 90°/–45° interfaces is first noted at the 0.0115-inch end displacement, as presented in Figure 3.33 (d) and (e). Subsequently, the first matrix damages are observed at the end displacement of 0.0138 inches in the 0° and ±45° layers, and are presented in Figure 3.34 (b) and (c), and Figure 3.34 (d) and (e), respectively. The matrix damages begin to extend into the 90° layers at the end displacement of

0.0165 inches, as presented in Figure 3.35 (f) and (g). Matrix damages and delaminations continue to propagate further in a very uniform fashion for the increasing end displacement levels of 0.0184, 0.0214 and 0.0306 inches, as presented in Figures 3.36 through 3.38, respectively. No fiber damage is noted up to the end displacement of 0.0306 inches.

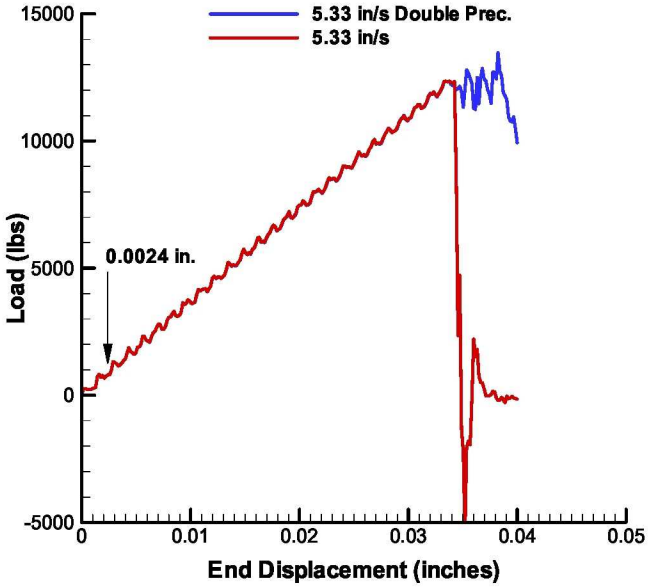

(a) End displacement of 0.0024 inches.

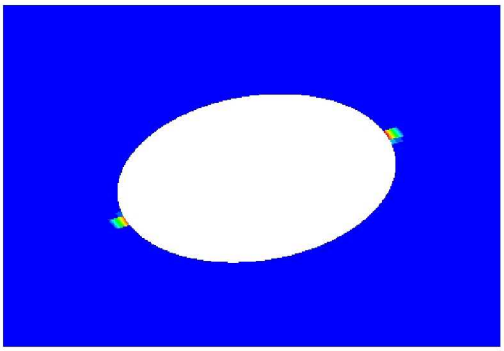

(b) Single precision solver.

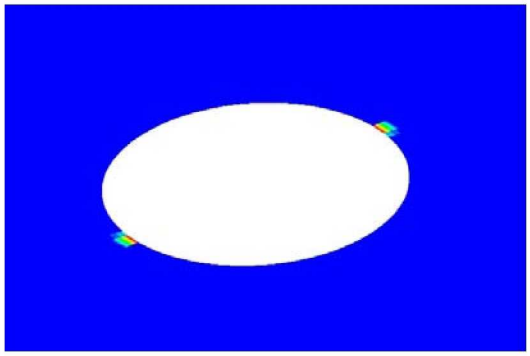

(c) Double precision solver.

Figure 3.32. End displacement of 0.0024 inches and initial delamination in the –45°/0° interface obtained using single precision and double precision solver.

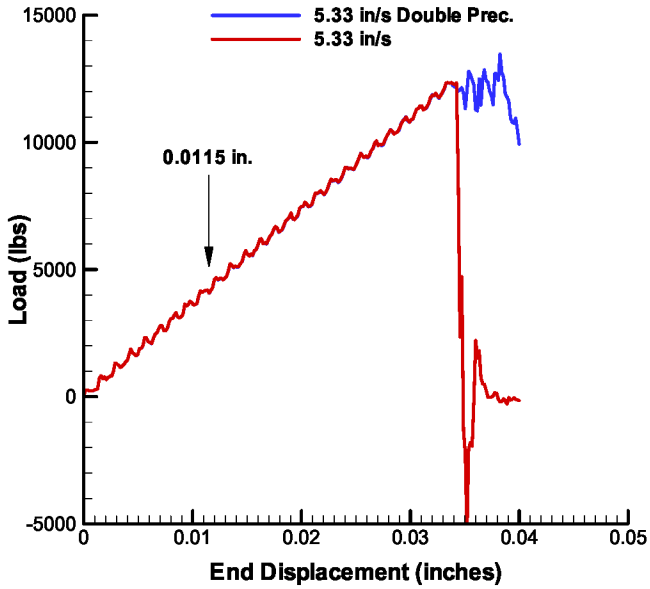

(a) End displacement of 0.0115 inches.

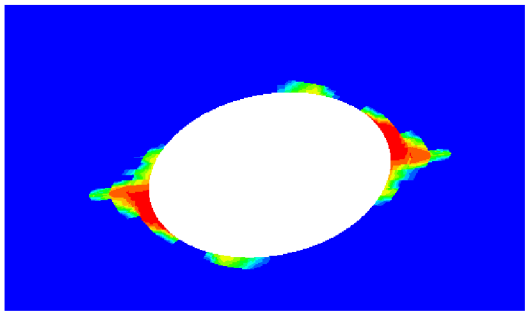

(b) Single precision solver.

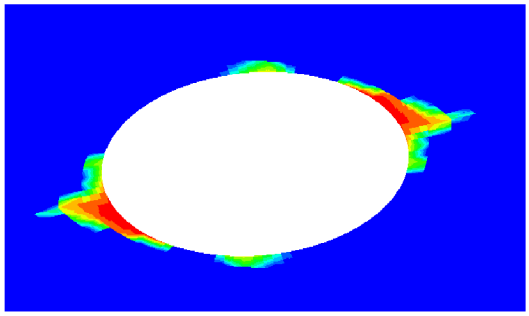

(c) Double precision solver.

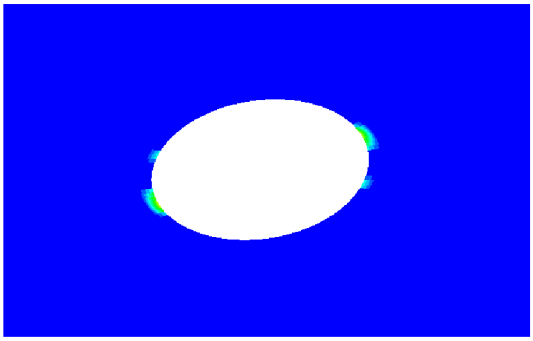

(d) Single precision solver.

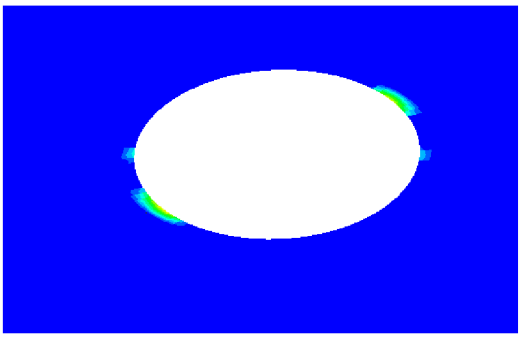

(e) Double precision solver.

Figure 3.33. End displacement of 0.0115 inches; delamination in the –45°/0° interface obtained using (b) single precision and (c) double precision solver; delamination in the 90°/–45° interface obtained using (d) single precision and (e) double precision solver.

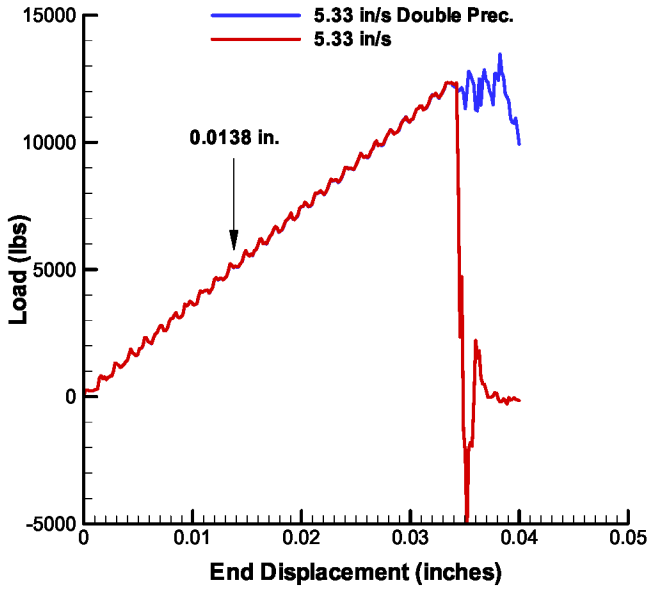

(a) End displacement of 0.0138 inches.

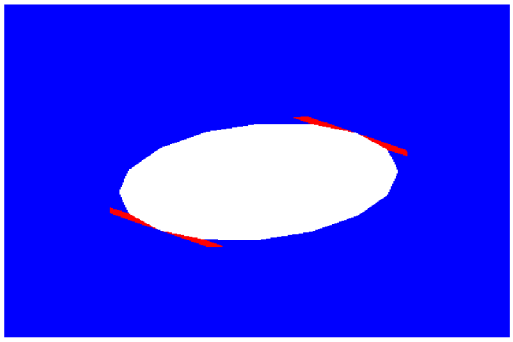

(b) Single precision solver.

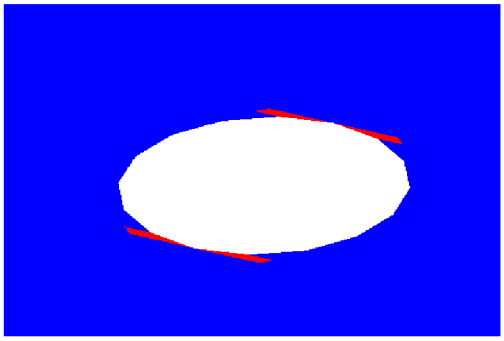

(c) Double precision solver.

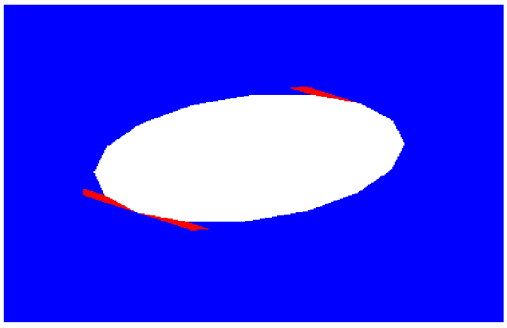

(d) Single precision solver.

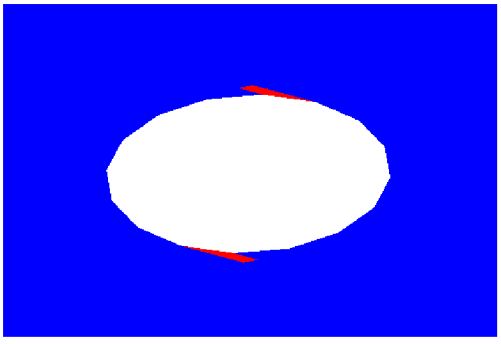

(e) Double precision solver.

Figure 3.34. End displacement of 0.0138 inches; matrix damage in the 0° layer obtained using (b) single precision and (c) double precision solver; matrix damage in the –45° layer obtained using (d) single precision and (e) double precision solver.

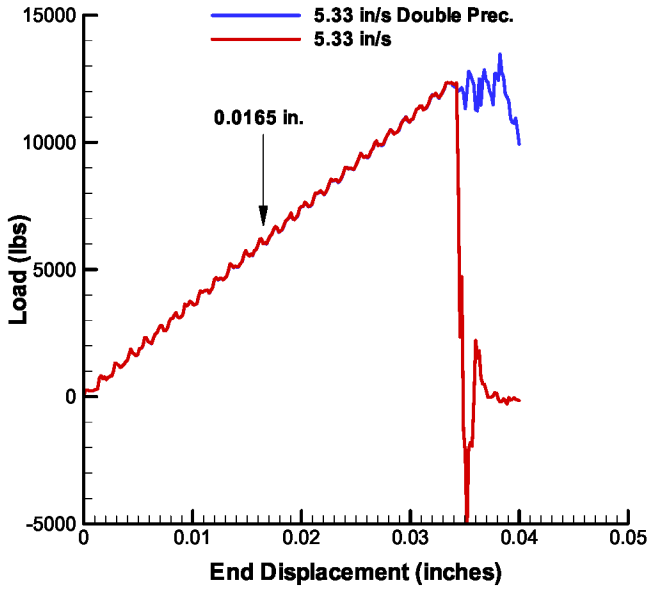

(a) End displacement of 0.0165 inches.

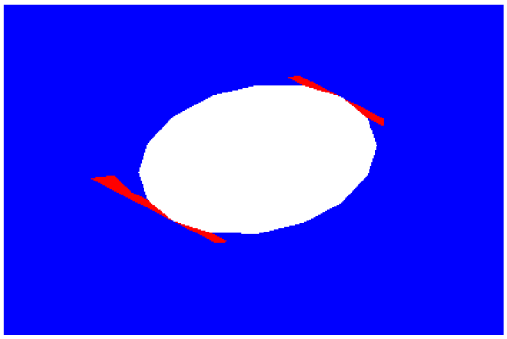

(b) Single precision solver.

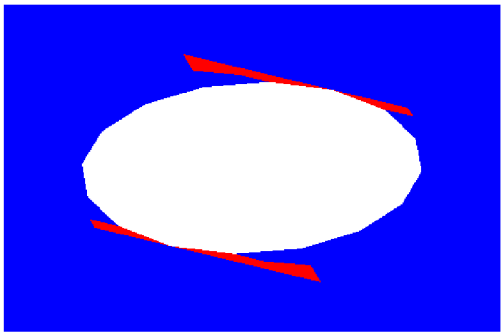

(c) Double precision solver.

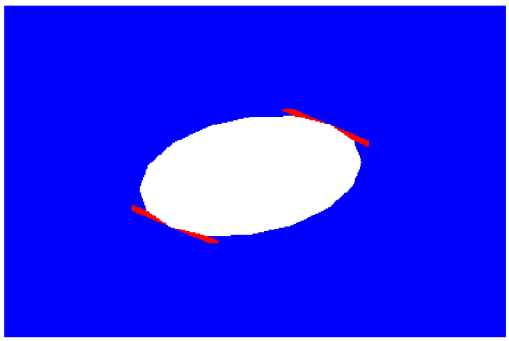

(d) Single precision solver.

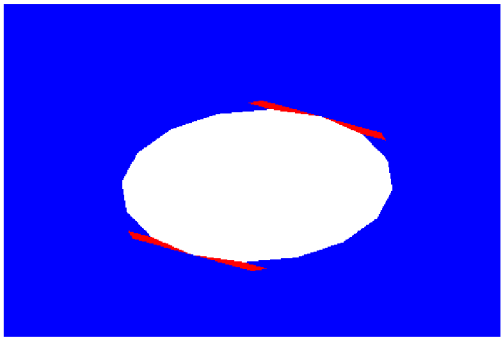

(e) Double precision solver.

Figure 3.35. End displacement of 0.0165 inches; matrix damage in the 0° layer obtained using (b) single precision and (c) double precision solver; matrix damage in the –45° layer obtained using (d) single precision and (e) double precision solver.

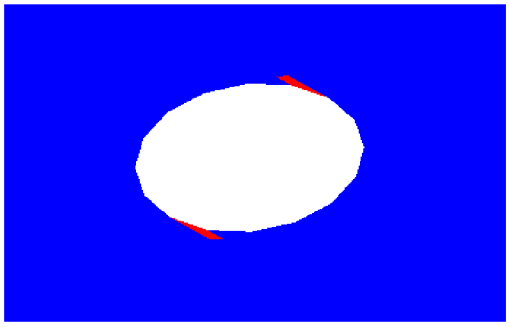

(f) Single precision solver.

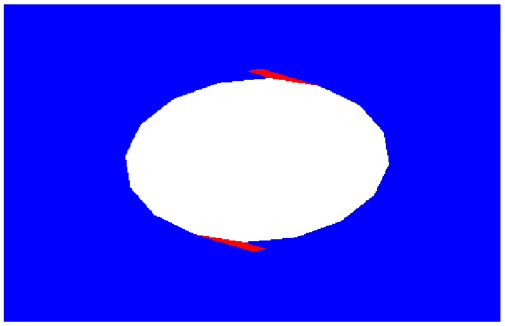

(g) Double precision solver.

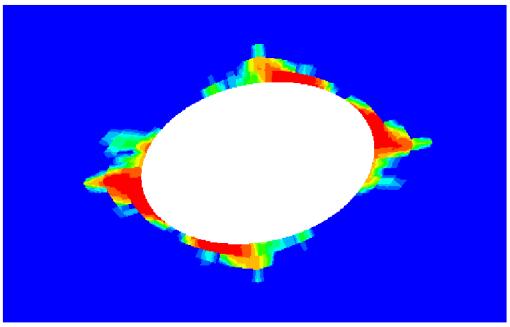

(h) Single precision solver.

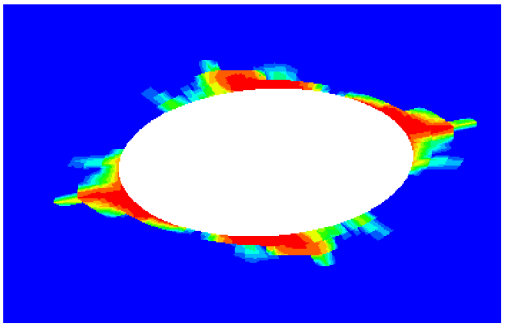

(i) Double precision solver.

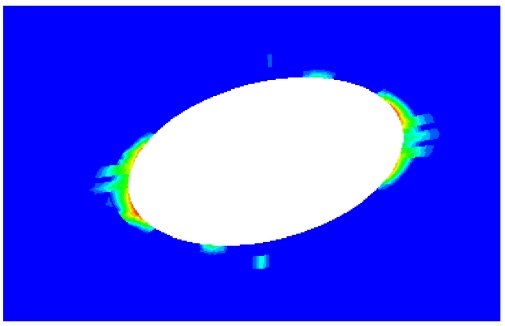

(j) Single precision solver.

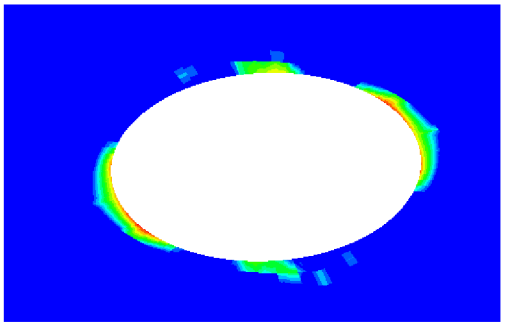

(k) Double precision solver.

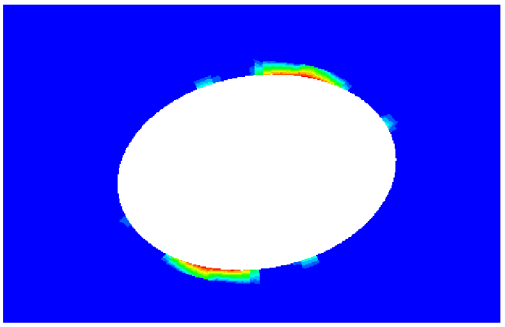

(l) Single precision solver.

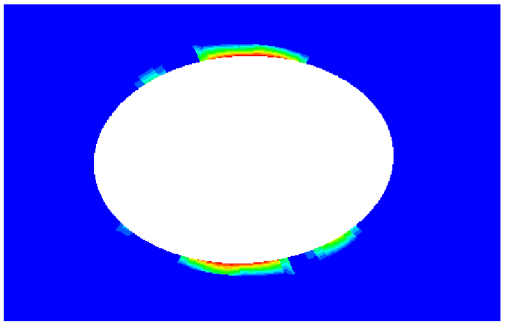

(m) Double precision solver.

Figure 3.35 (concluded). End displacement of 0.0165 inches; matrix damage in the 90° layer obtained using (f) single precision and (g) double precision solver; delamination in the 0°/–45° interface obtained using (h) single precision and (i) double precision solver; delamination in the –45°/90° interface obtained using (j) single precision and (k) double precision solver; delamination in the 90°/45° interface obtained using (l) single precision and (m) double precision solver.

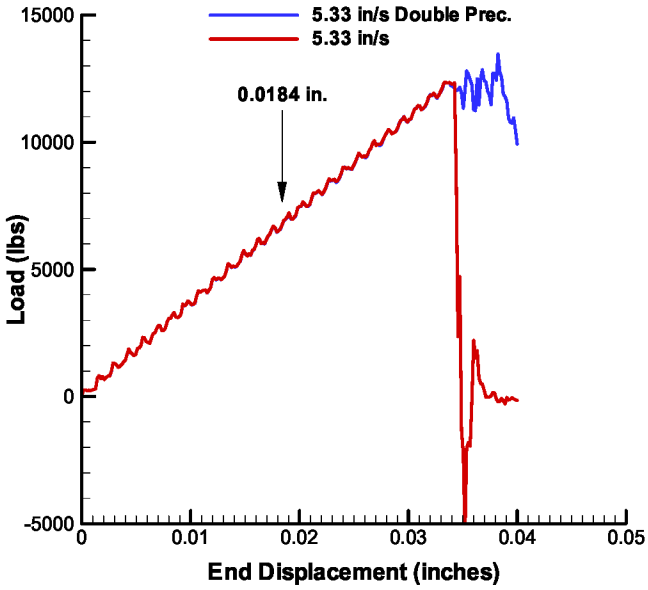

(a) End displacement of 0.0184 inches.

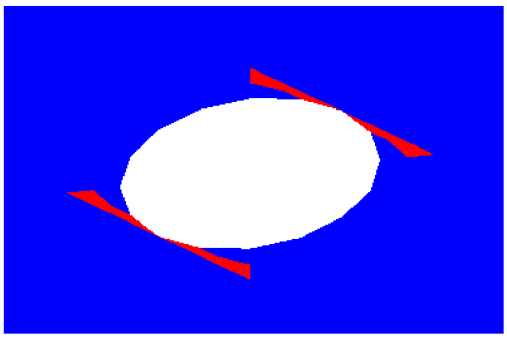

(b) Single precision solver.

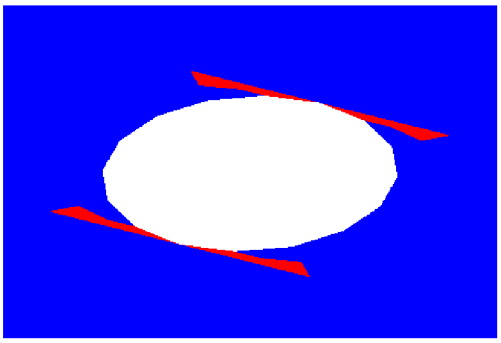

(c) Double precision solver.

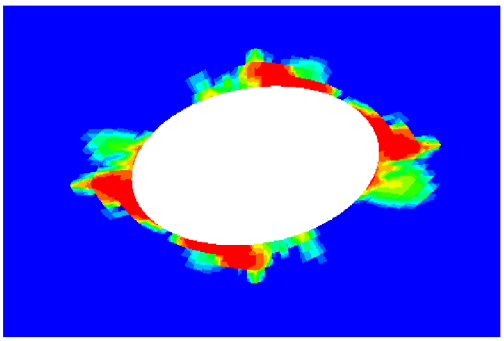

(d) Single precision solver.

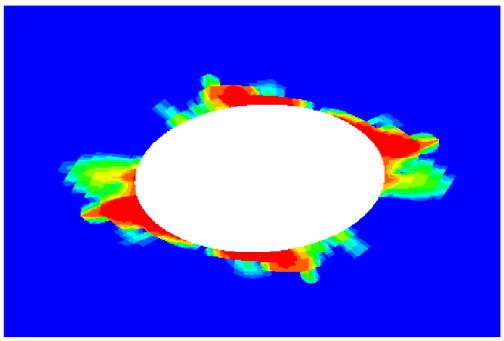

(e) Double precision solver.

Figure 3.36. End displacement of 0.0184 inches; matrix damage in the 0° layer obtained using (b) single precision and (c) double precision solver; delamination in the 0°/–45° interface obtained using (d) single precision and (e) double precision solver.

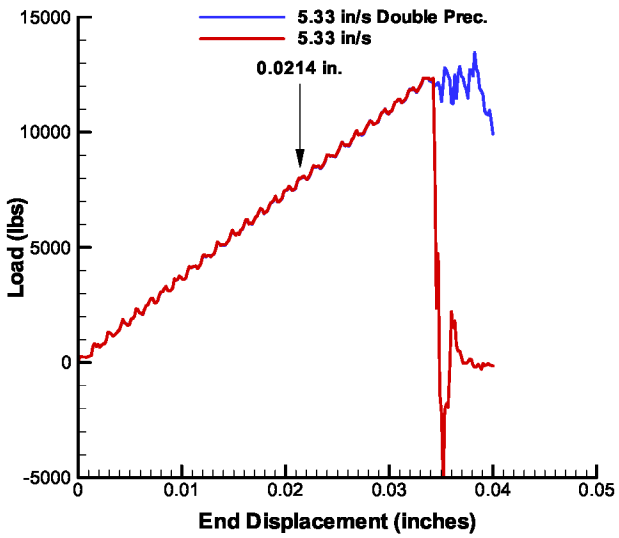

(a) End displacement of 0.0214 inches.

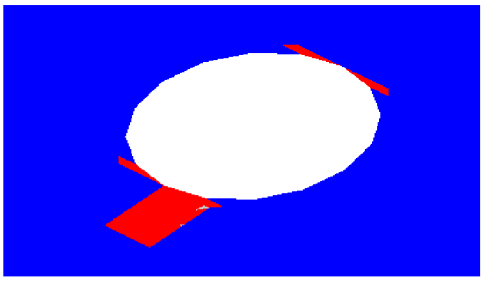

(b) Single precision solver.

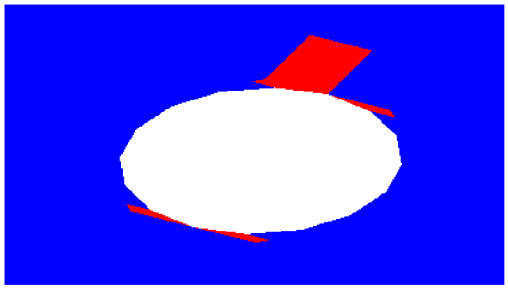

(c) Double precision solver.

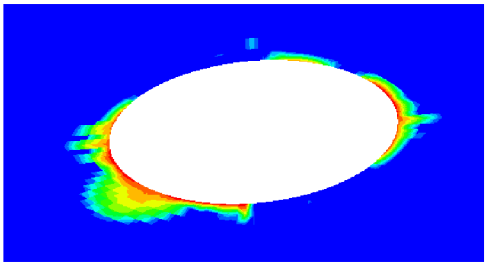

(d) Single precision solver.

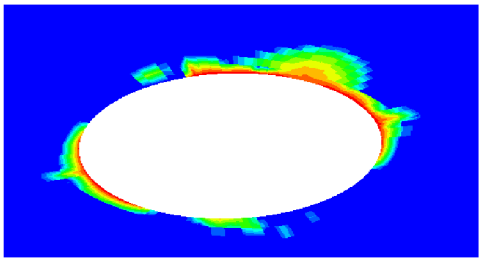

(e) Double precision solver.

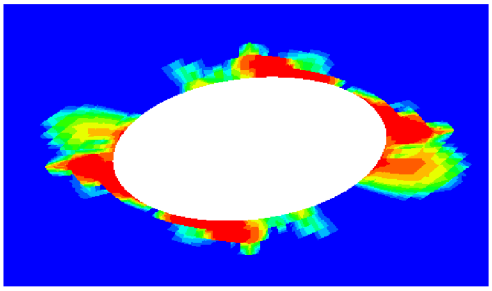

(f) Single precision solver.

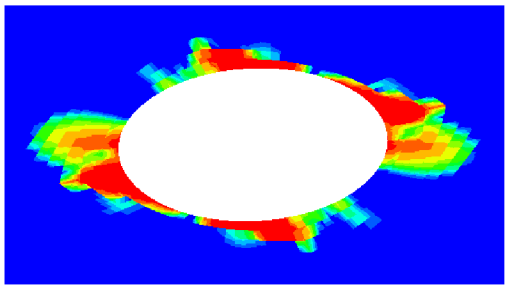

(g) Double precision solver.

Figure 3.37. End displacement of 0.0214 inches; matrix damage in the 90° layer obtained using (b) single precision and (c) double precision solver; delamination in the 90°/–45° interface obtained using (d) single precision and (e) double precision solver; delamination in the –45°/0° interface obtained using (f) single precision and (g) double precision solver.

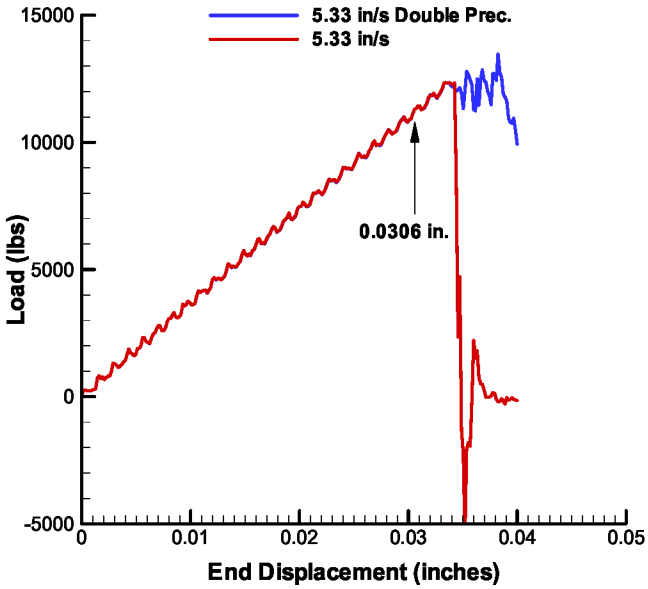

(a) End displacement of 0.0306 inches.

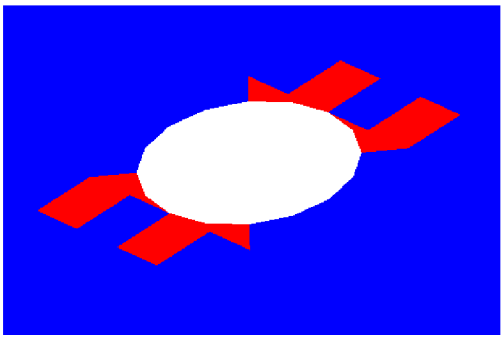

(b) Single precision solver.

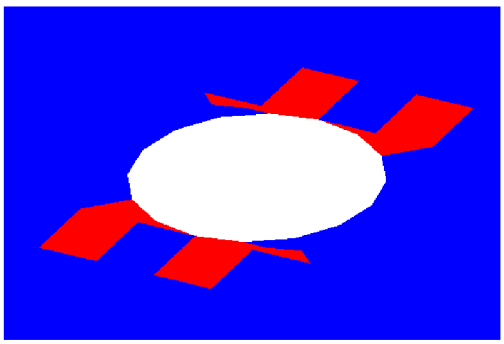

(c) Double precision solver.

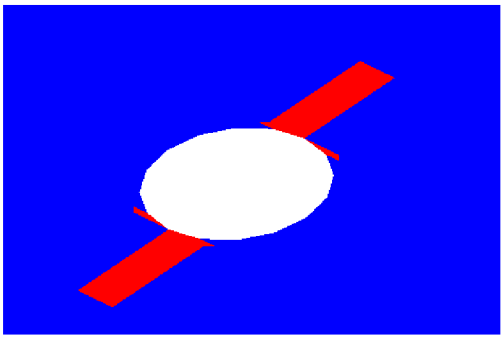

(d) Single precision solver.

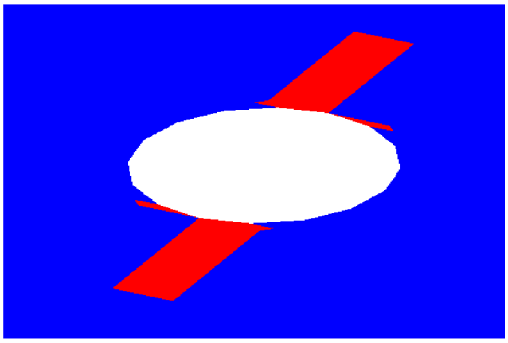

(e) Double precision solver.

Figure 3.38. End displacement of 0.0306 in.; matrix damage in the –45° layer obtained using (b) single precision and (c) double precision solver; matrix damage in the 90° layer obtained using (d) single precision and (e) double precision solver.

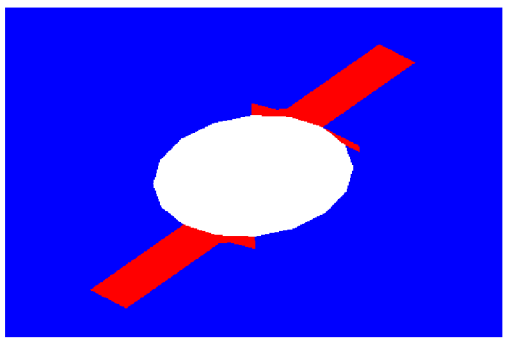

(f) Single precision solver.

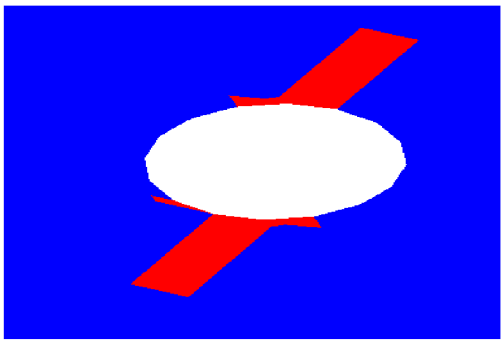

(g) Double precision solver.

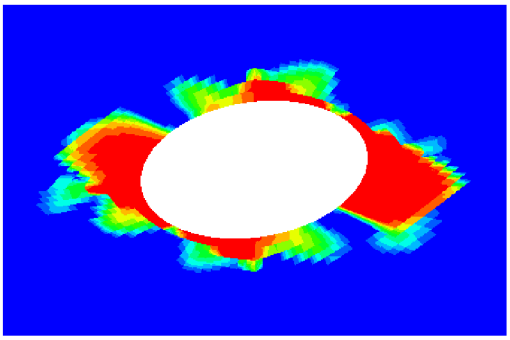

(h) Single precision solver.

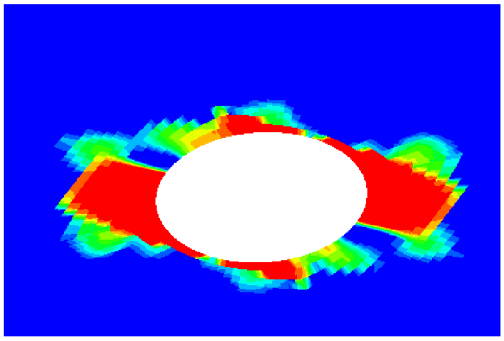

(i) Double precision solver.

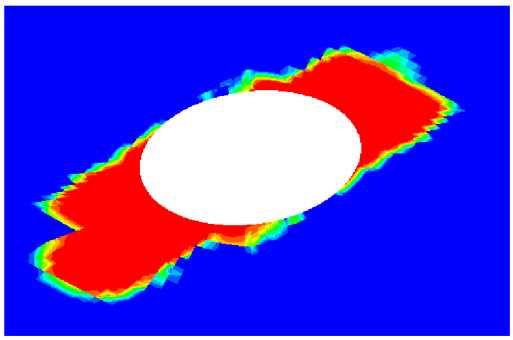

(j) Single precision solver.

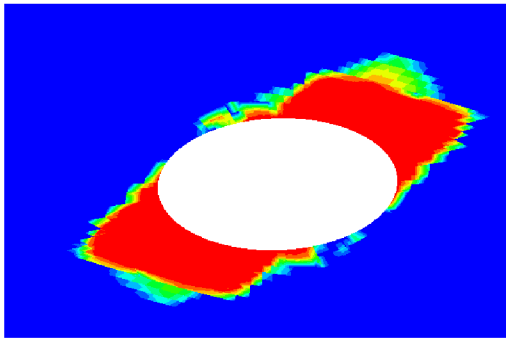

(k) Double precision solver.

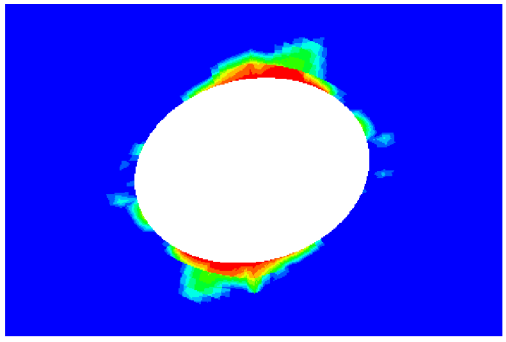

(l) Single precision solver.

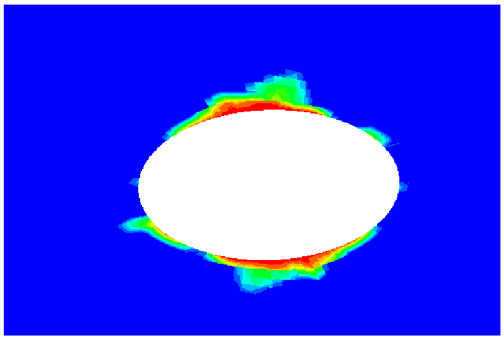

(m) Double precision solver.

Figure 3.38 (concluded). End displacement of 0.0306 inches; matrix damage in the 45° layer obtained using (f) single precision and (g) double precision solver; delamination in the 0°/–45° interface obtained using (h) single precision and (i) double precision solver; delamination in the –45°/90° interface obtained using (j) single precision and (k) double precision solver; delamination in the 90°/45° interface obtained using (l) single precision and (m) double precision solver.

However, as the two solutions approach the maximum loading and at the same time exceed approximately 300,000 iterations, they begin to diverge. The first noticeable difference between the single and double precision solutions is illustrated for the end displacement of 0.0339 inches seen in Figure 3.39. It is seen in Figure 3.39 (d) and (f) that the single precision solution yields initial fiber damage in the 0° plies while the double precision solution does not show any fiber damage yet, as seen in Figure 3.39 (e). At this load level, matrix damage (Figure 3.39 (b) and (c)) and delamination (Figure 3.39 (g) and (h)) are present in both solutions, but the pattern and extent of these damages differs. Despite these observations, the overall load versus end displacement curve obtained with both solvers, presented in Figure 3.39 (a), is still nearly identical up to this load level signifying that the load-carrying capability of the sub-critically damaged structure is very similar according the two solvers.

The differences in damages for fiber, matrix and delamination magnify further at the end displacement of 0.0344 inches presented in Figure 3.40. Fiber damage obtained with the single precision solver compromises the entire 0° ply at the mid-span location as presented in Figure 3.40 (d), while the fiber remains undamaged in the double precision solution shown in Figure 3.40 (e). The extent of matrix damage (Figure 3.40 (b) and (c)) and delamination (Figure 3.40 (f) and (g)) is not only more significant than at the 0.0339-inch end displacement, but also the differences in patterns are more significant. Therefore, it comes as no surprise that the load corresponding to the two solutions at the 0.0344-inch displacement differs vastly, as presented in Figure 3.40 (a). Due to the 0° plies' fiber failure, the single precision solution results show a rapid decrease in the load-carrying capability, while the double precision solution, after a slight initial drop associated with the matrix damages and delamination, further increases the load-carrying capability.

At the end displacement of 0.0363 inches, the single precision solution indicates nearly a total loss of load-carrying capability while the double precision solver yields a solution still only slightly below the peak load, as presented in Figure 3.41 (a). The double precision solver shows considerable matrix damage, especially in the 0° ply as presented in Figure 3.41 (b), and delamination, especially in the –45°/0° interfaces as presented in Figure 3.41 (d). The double precision solution still yields undamaged fiber as presented in Figure 3.41 (c).

Finally, the double precision solution at the end displacement of 0.0390 inches, i.e., past its peak load, is presented in Figure 3.42. While matrix damage is substantial (see Figure 3.42 (b)), and even some fiber is tagged as damaged due to an excessive strain level (Figure 3.42 (c) and (d)), the final damage mode is attributed to extensive delamination (Figure 3.42 (e)).

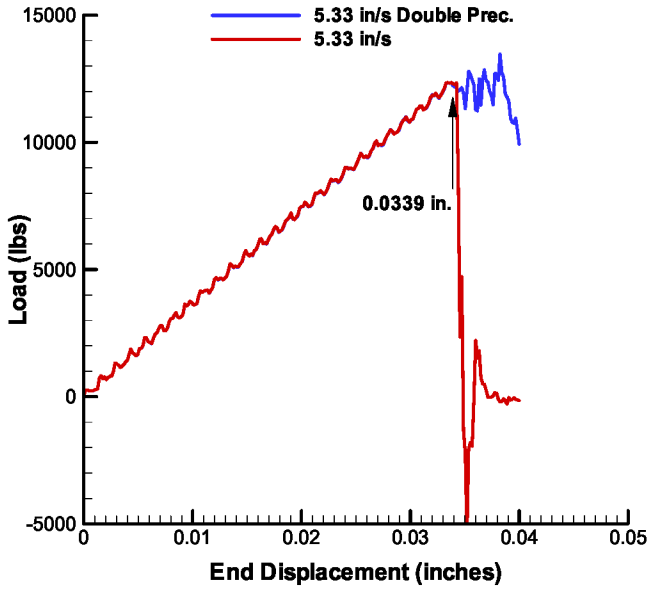

(a) End displacement of 0.0339 inches.

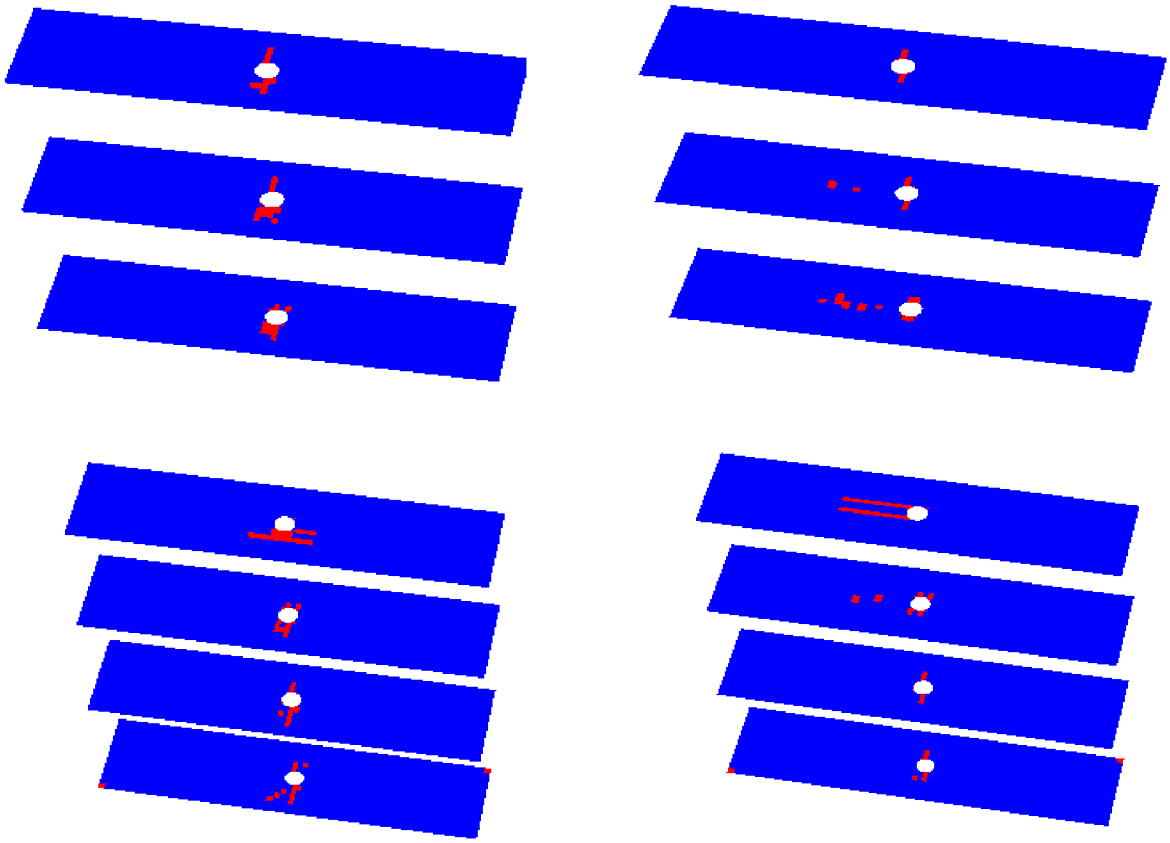

(b) Single precision solver.

(c) Double precision solver.

Figure 3.39. End displacement of 0.0339 inches; matrix damage obtained using (b) single precision and (c) double precision solver for all layers.

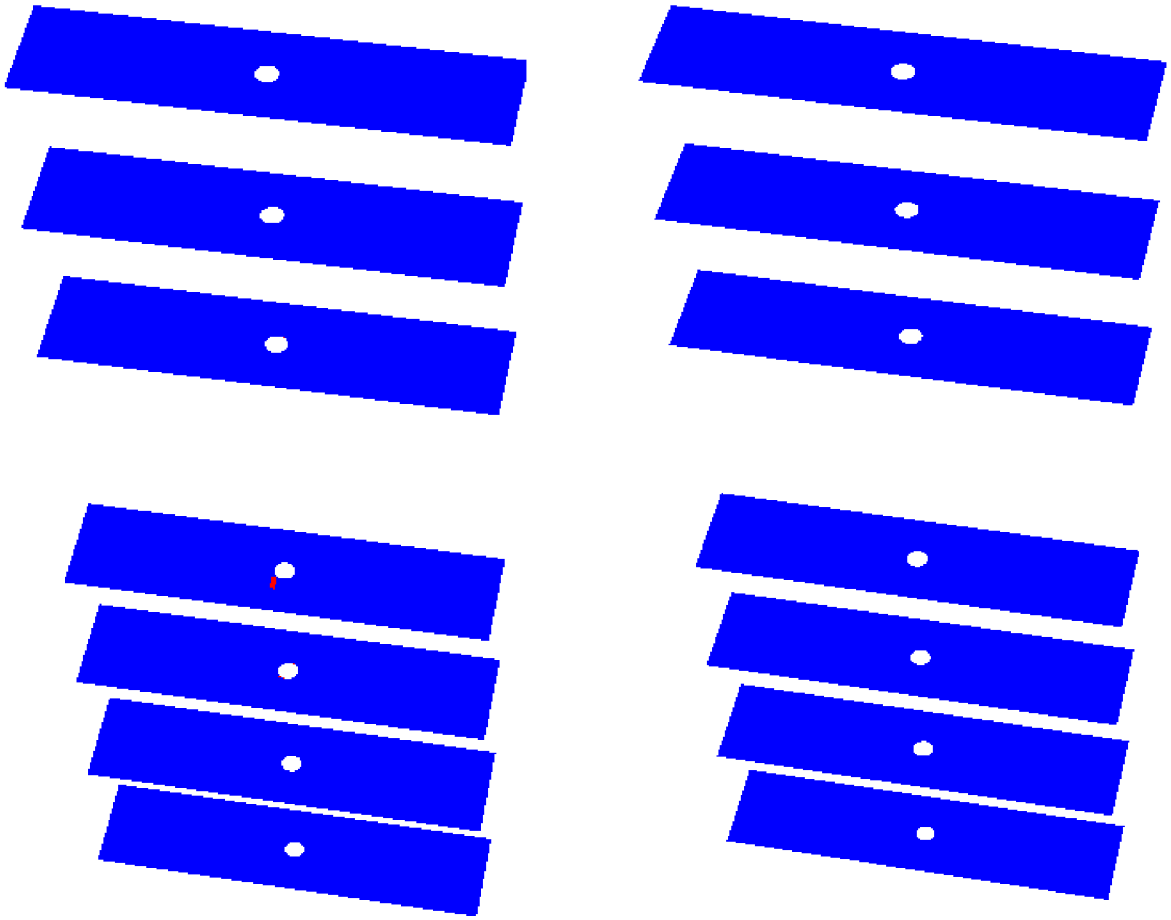

(d) Single precision solver.

(e) Double precision solver.

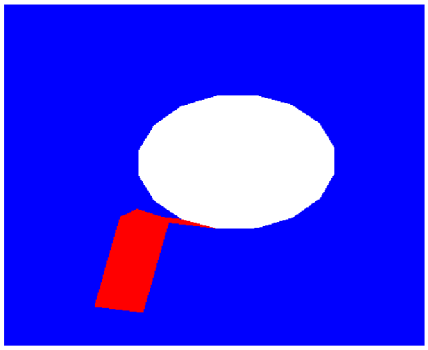

(f) Single precision solver.

Figure 3.39 (continued). End displacement of 0.0339 inches; fiber damage obtained using (d) single precision and (e) double precision solver for all layers; (f) zoomed-in fiber damage in the 0° layer obtained using single precision solver.

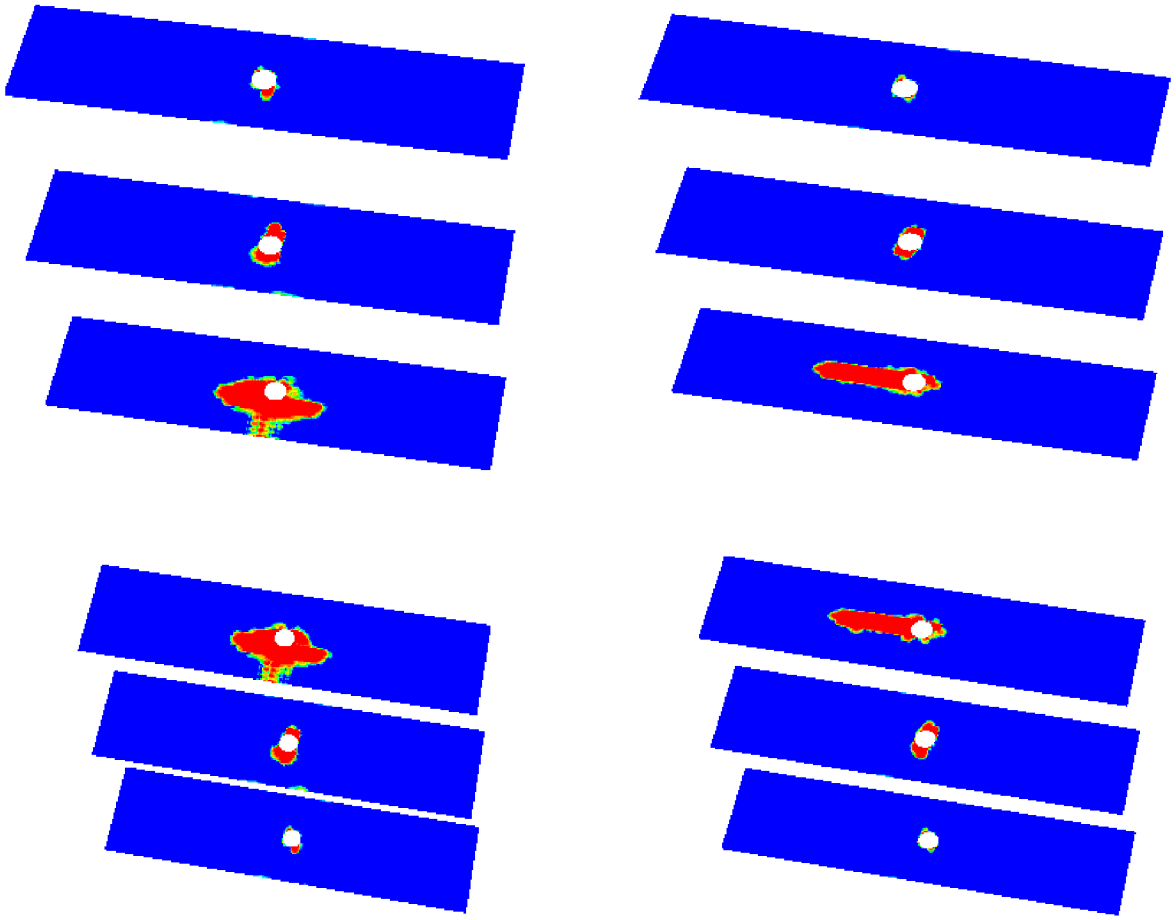

(g) Single precision solver.

(h) Double precision solver.

Figure 3.39 (concluded). End displacement of 0.0339 inches; delamination obtained using (g) single precision and (h) double precision solver for all interfaces.

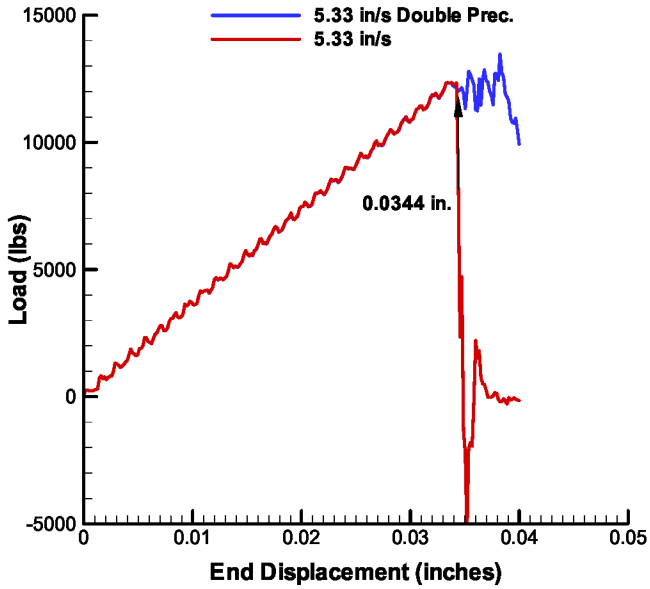

(a) Specimen end displacement of 0.0344 inches.

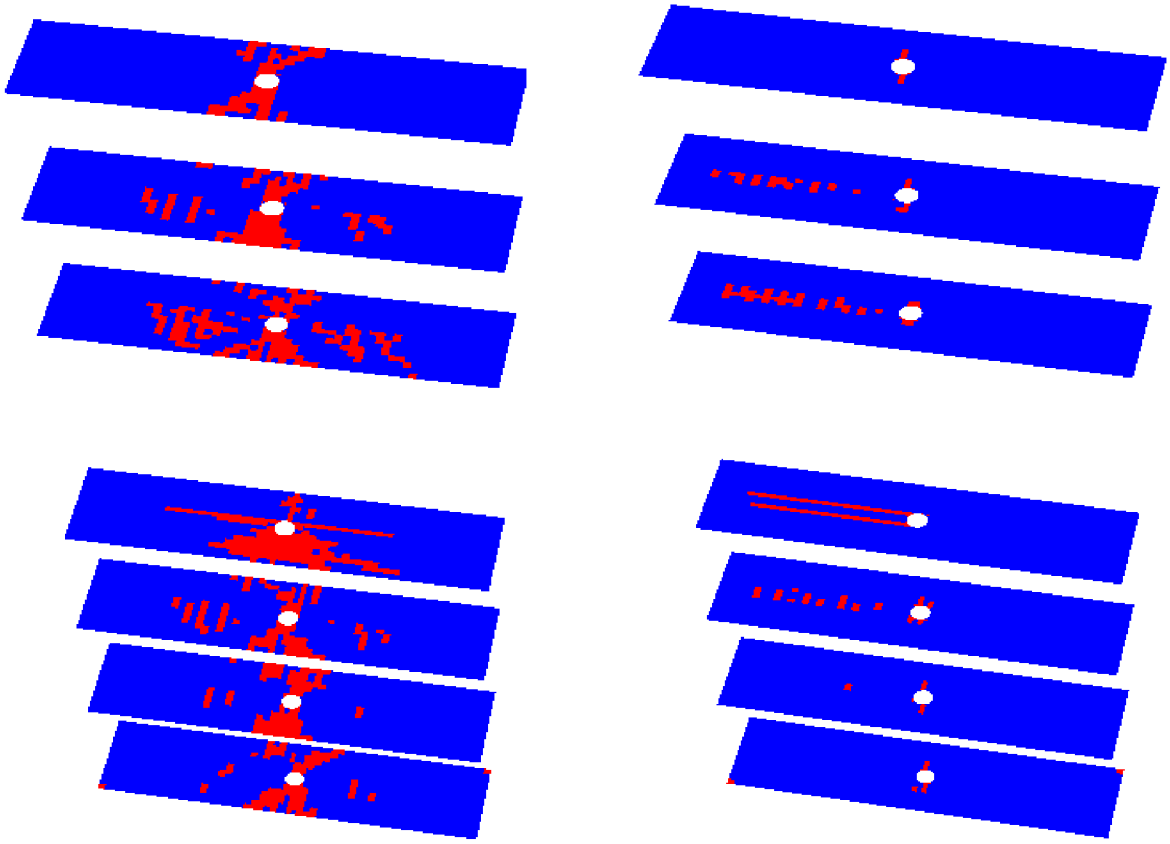

(b) Single precision solver.

(c) Double precision solver.

Figure 3.40. Specimen end displacement of 0.0344 inches; matrix damage obtained using (b) single precision and (c) double precision solver for all layers.

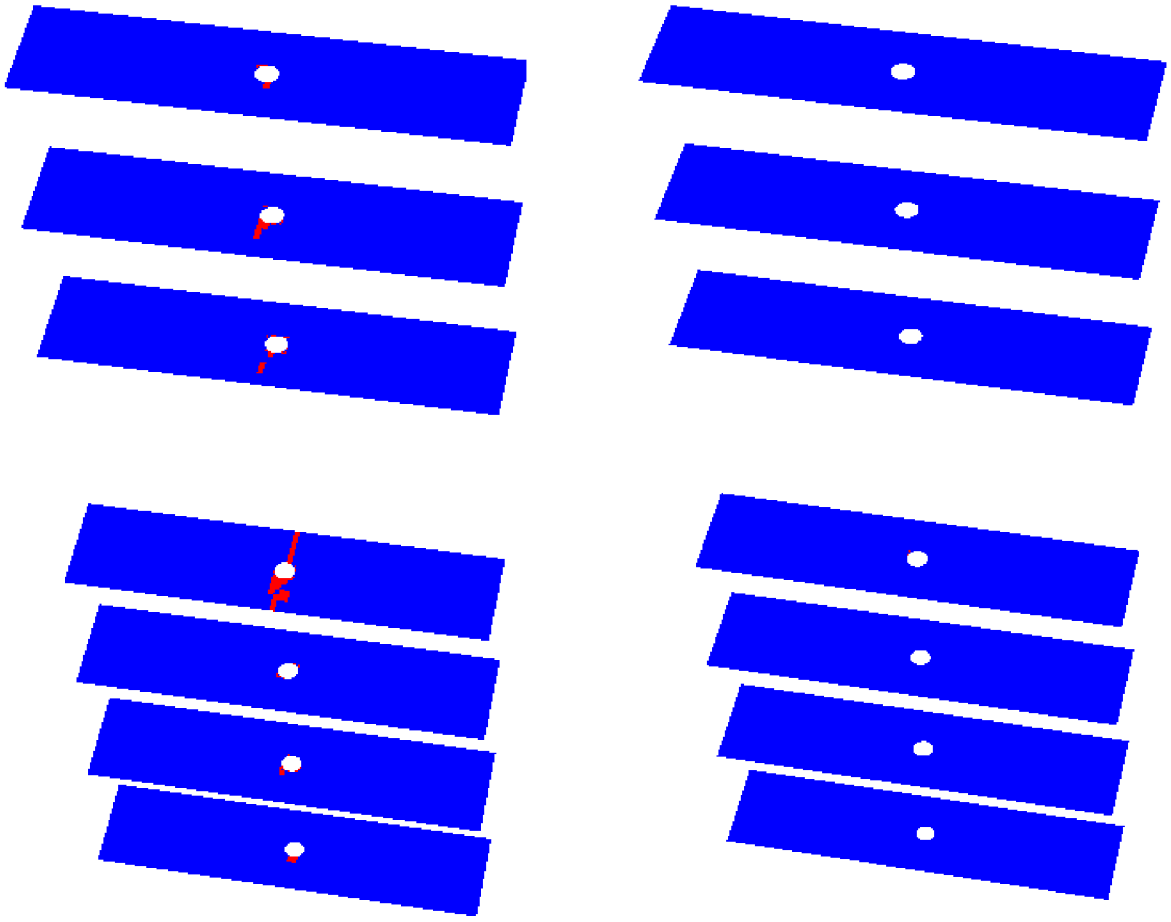

(d) Single precision solver.

(e) Double precision solver.

Figure 3.40 (continued). End displacement of 0.0344 inches; fiber damage obtained using (d) single precision and (e) double precision solver for all layers.

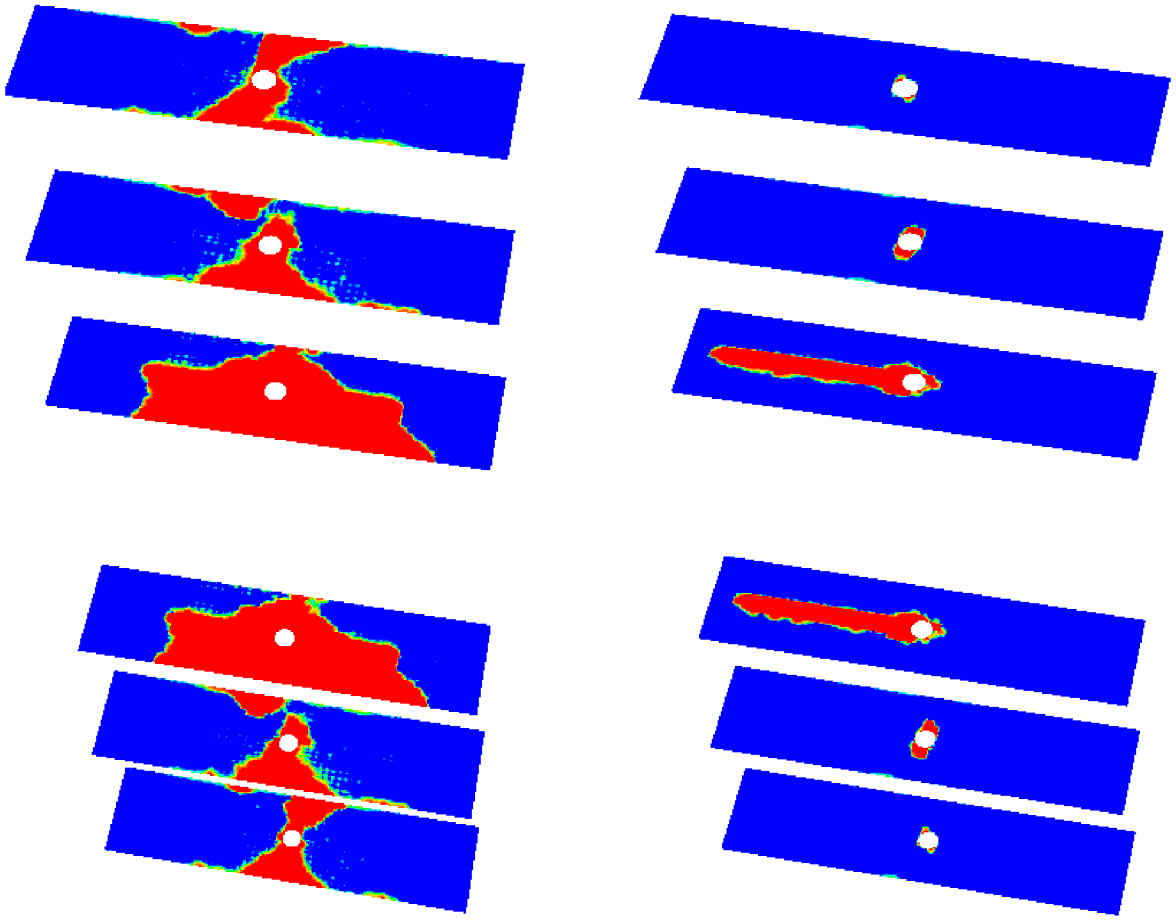

(f) Single precision solver.

(g) Double precision solver.

Figure 3.40 (concluded). End displacement of 0.0344 inches; delamination obtained using (f) single precision and (g) double precision solver for all interfaces.

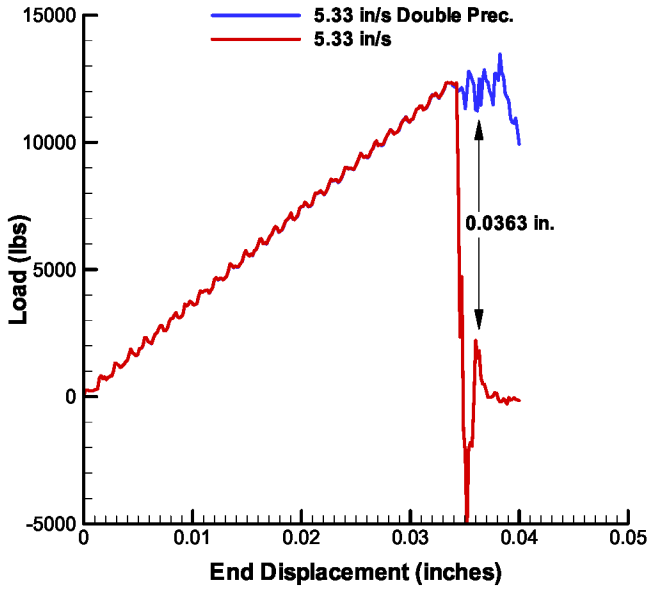

(a) Specimen end displacement of 0.0363 inches.

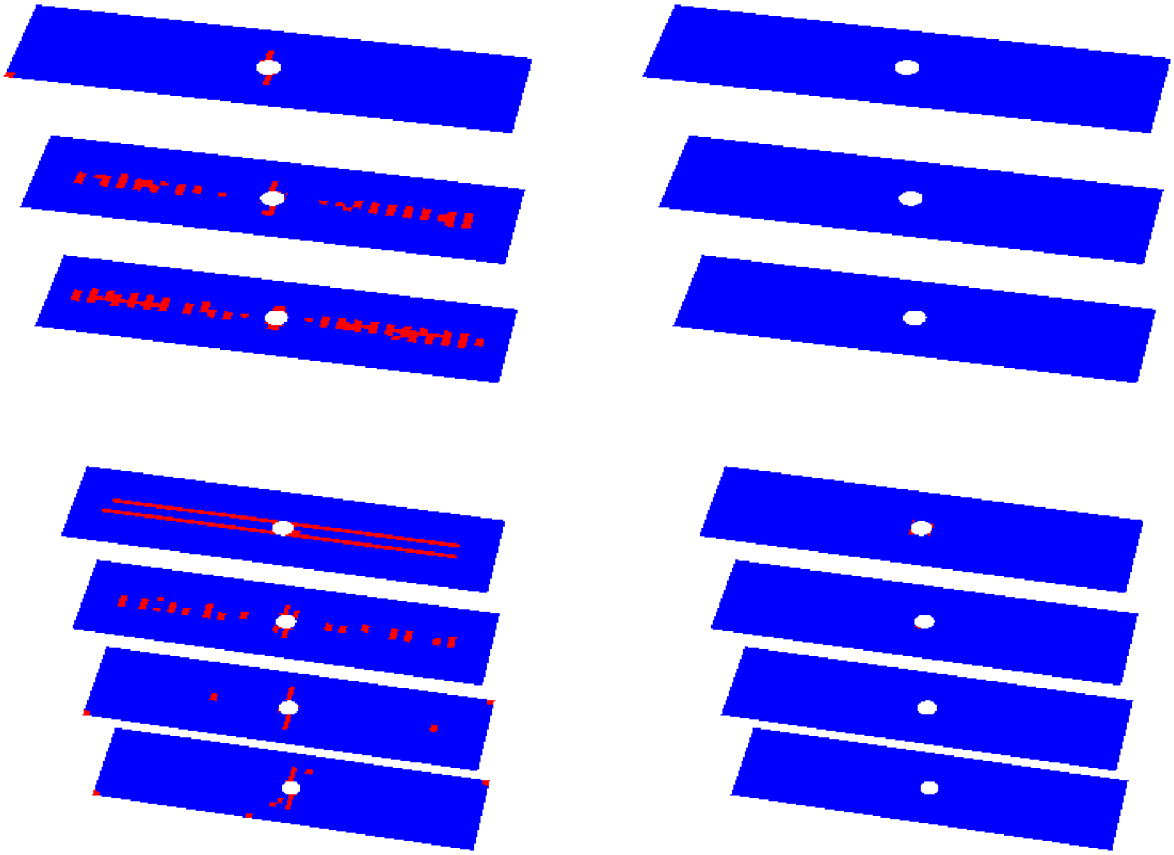

(b) Single precision solver.

(c) Double precision solver.

Figure 3.41. End displacement of 0.0363 inches; (b) matrix damage and (c) fiber damage obtained using double precision solver.

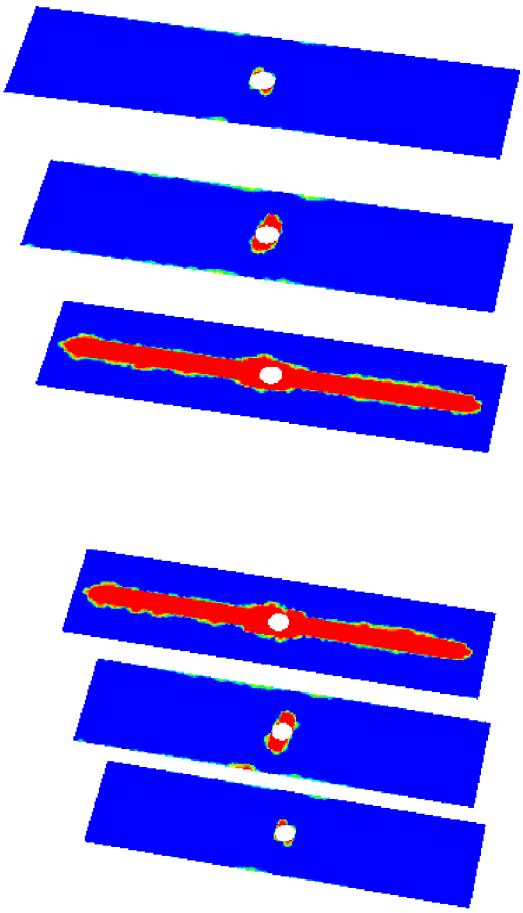

(d) Double precision solver.

Figure 3.41 (concluded). End displacement of 0.0363 inches; (d) delamination obtained using double precision solver.

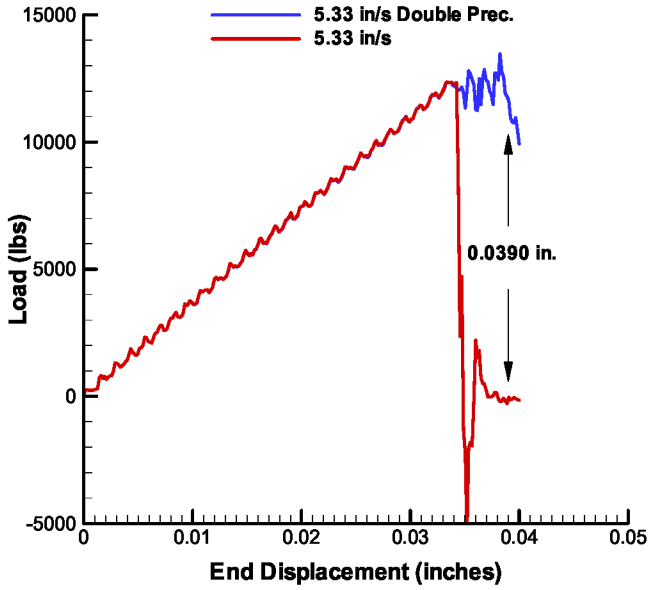

(a) Specimen end displacement of 0.0390 inches.

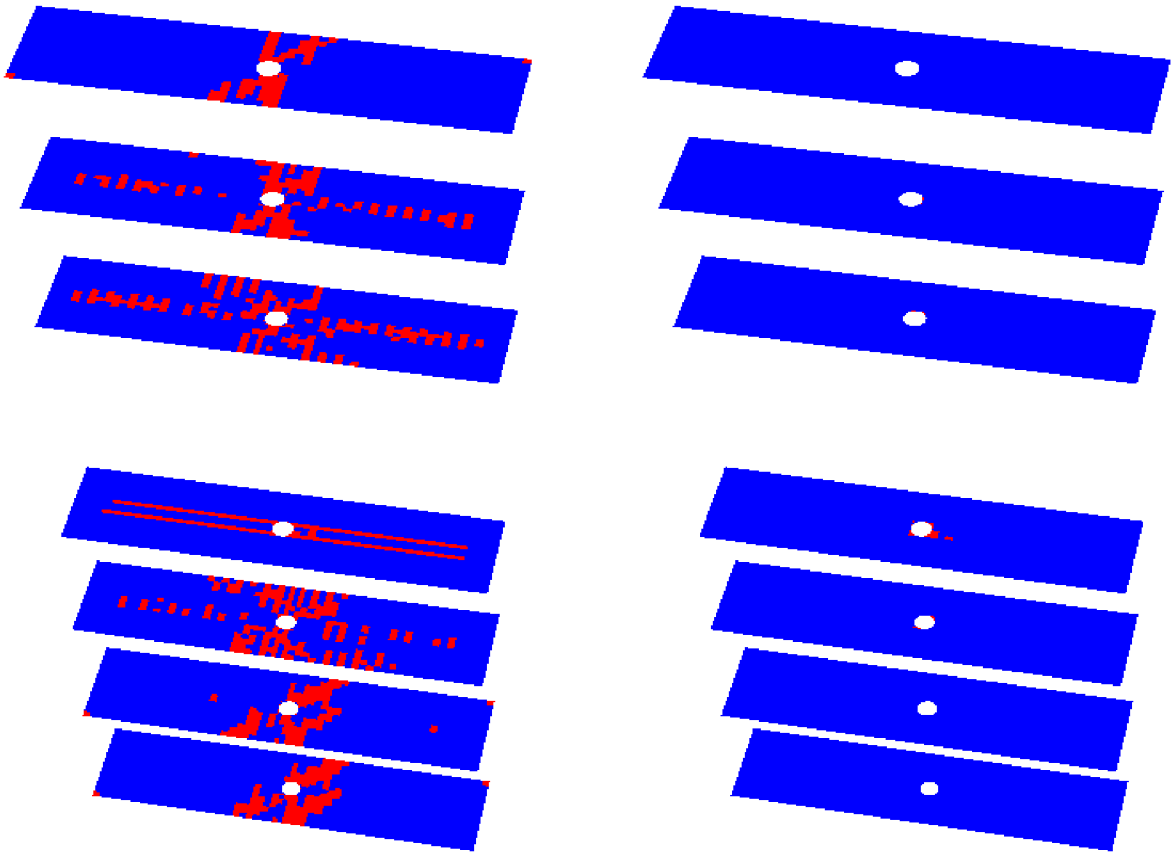

(b) Matrix damage obtained using double precision solver.

(c) Fiber damage obtained using double precision solver.

Figure 3.42. End displacement of 0.0390 inches; (b) matrix damage and (c) fiber damage obtained using double precision solver.

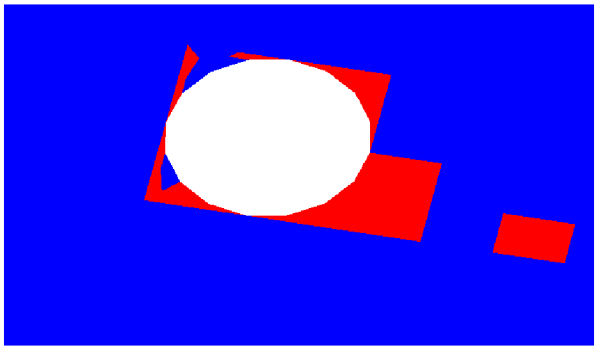

(d) Zoomed-in fiber damage in the 0° layer

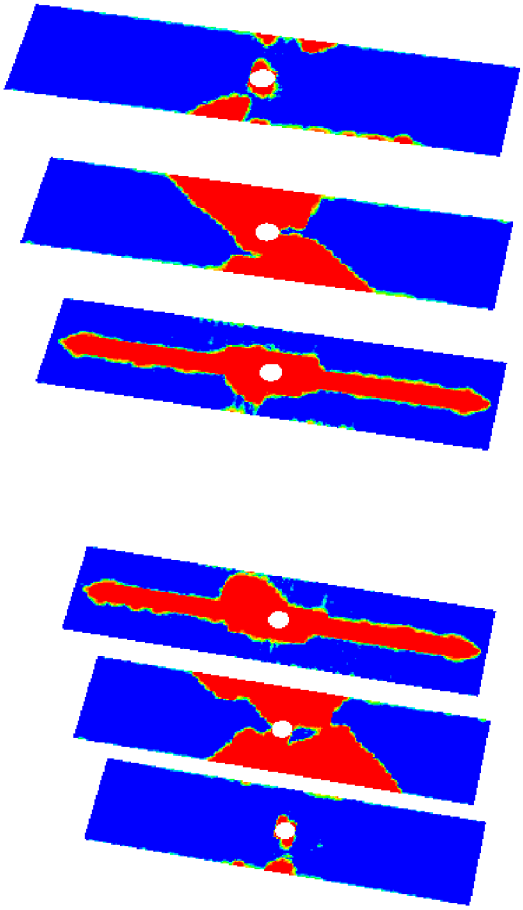

(e) Delamination obtained using double precision solver

Figure 3.42 (concluded). End displacement of 0.0390 inches; (d) zoomed-in fiber damage in the 0° layer and (e) delamination obtained using double precision solver.

The same pull-out damage was predicted for the 8-ply laminate from the two different loading rate analyses, even though the faster loading rate case required fewer than 300,000 iterations and the slower loading rate case required more than 300,000 iterations. The load versus end displacement curves for these two cases are presented in Figure 3.43 and indicate the same type of instantaneous failure occurring at almost the same load level. This comparison shows that the failure type in this specific case is well defined and, consequently, is not sensitive to the round-off error accumulating faster in the single precision solution. To verify such a hypothesis, further investigation revealed that in the 8-ply laminate shear stresses in 0° ply were lagging behind the axial stresses, and the later stress reached its failure limit first causing the failure of the laminate.

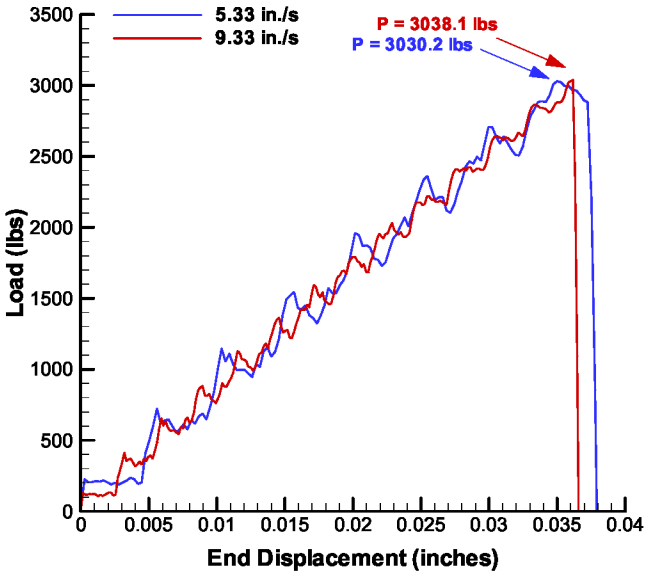

Figure 3.43. Load versus end displacement of a $[45/90/-45/0]_s$ laminate with a 0.25-inch-diameter hole.

4.0 Conclusions

The PFA methodology with COSTR damage model has been presented. Failure types and failure loads in a carbon-epoxy $[45_n/90_n/-45_n/0_n]_{ms}$ laminate coupons with central circular holes in tensile load were predicted and compared with published test results. The COSTR damage model was able to accurately predict the failure stress, damage modes, and failure type in the ply-level and sub-laminate-level stacked laminates considered.

Brittle, pull-out, and delamination damage types exhibited by 8-, 16-, and 32-ply-thick ply-level scaled specimens with a 0.25-inch-diameter hole were captured very well with the COSTR damage model. The damage modes such as fiber failure, matrix failure and delamination failure for all the three types of damage have been found to agree with the observations provided in Ref. 24. The splitting in the 0° plies of the 32-ply laminate was very well captured along with the load level at which this phenomenon occurs. Similar conclusions regarding the accuracy of the COSTR model were reached based on the 0.5-inch-diameter hole examples. Specifically, for the 32-ply thick laminate, the characteristics of a brittle type of damage (such as a clean fractured surface, fiber failure in all the plies, and the confinement of matrix damage and delamination to the crack path only) were all captured and matched very well the explanation provided in Ref. 24.

In this study, the in-plane modeling parameters, such as mesh size and shape around the discontinuous regions, were maintained approximately constant regardless of the size and thickness of the specimen and no adverse consequences of such an approach were noted.

Finally, the sensitivity of a predicted failure type and damage modes to single and double precision explicit solvers has been investigated. Application of the double precision solver was determined necessary for performing progressive damage analysis which requires more than 300,000 iterations. A detrimental effect of single precision solution round-off errors on a predicted damage type has been clearly demonstrated. When the estimated number of required iterations is not known prior to the analysis, application of the double precision solver is recommended.

References

1. Knight, N. F., Jr.: "Factors Influencing Progressive Failure Analysis Predictions for Laminated Composite Structure." *Proceedings of the 49th AIAA/ASME/ASCE/AHS/ASC Structures, Structural Dynamics, and Materials Conference*, Schaumburg, Illinois, April 2008, AIAA-2008-2108.
2. Chang, F. K.; and Chang, K. Y.: "A Progressive Damage Model for Laminated Composites Containing Stress Concentrations." *Journal of Composite Materials*, Vol. 21, September 1987.
3. Chang, F. K.; and Lessard, L.: "Damage Tolerance of Laminated Composites Containing an Open Hole and Subjected to Compressive Loadings: Part I – Analysis." *Journal of Composite Materials*, Vol. 25, January 1991.
4. Tan, S.: "A Progressive Failure Model for Composite Laminates Containing Openings." *Journal of Composite Materials*, Vol. 25, May 1991.
5. Gama, B. A.; Xiao, J. R.; Hague, M. J.; Yen, C. F.; and Gillespie, J. W., Jr.: "Experimental and Numerical Investigations on Damage and Delamination in Thick Plain Weave S-2 Glass Composites Under Quasi-Static Punch Shear Loading." *18th Annual Technical Conference of American Society for Composites*, University of Florida, Gainesville, Florida, October 2003.
6. Davies, G. A. O.; and Zhang, X.: "Impact Damage Prediction in Carbon Composite Structures." *International Journal of Impact Engineering,* Vol. 16, No. 1, 1995, pp. 149-170.
7. Yen, C. F.; and Cassin, T.: "Progressive Failure Analysis of Thin-Walled Composite Tubes Under Low Energy Impact." *Proceedings of the 39th AIAA/ASME/ASCE/AHS/ASC Structures, Structural Dynamics and Materials Conference*, Long Beach, California, April 1998, AIAA 98-1742, pp. 363-371.
8. Minnetyan, L.; and Abdi, F.: "Dynamic Impact Loading Damage Propagation in Composite Structures." *Proceedings of the 45th AIAA/ASME/ASCE/AHS/ASC Structures, Structural Dynamics and Materials Conference*, Palm Springs, California, April 2004, AIAA 2004-1688.
9. Yen, C. F.: "Analysis of Impact Damage Progression in Composite Structures." *Proceedings of the 5th LS-DYNA User Conference*, Southfield, Mississippi, September 1998.
10. Ambur, D. R.; Jaunky, N.; and Dávila, C. G.: "Progressive Failure of Composites' Laminates using LaRC02 Failure Criteria." *Proceedings of the 45th AIAA/ASME/ASCE/AHS/ASC Structures, Structural Dynamics, and Materials Conference*, Palm Springs, California, April 2004, AIAA 2004-1595-CP.
11. Qing, X; Chang, F. K.; and Starnes, J.: "Damage Tolerance of Notched Composite Laminates with Reinforcing Strips." *Journal of Composite Materials*, Vol. 37, No. 2, 2003.
12. Bogert, B. P.; Satyanarayana, A.; and Chunchu, B. P.: "Comparison of Damage Path Predictions for Composite Laminates by Explicit and Standard Finite Element Analysis Tools." *Proceedings of the 47th AIAA/ASME/ASCE/AHS/ASC Structures, Structural Dynamics and Materials Conference*, Newport, Rhode Island, May 2006, AIAA 2006-1750.
13. Camanho, P. P.; Maimi, P.; and Dávila, C. G.: "Prediction of Size Effects in Notched Laminates Using Continuum Damage Mechanics." *Composite Science and Technology 67*, 2007, pp. 2715-2727.
14. Lapczyk, I.; and Hurtado, J. A.: "Progressive Damage Modeling in Fiber-Reinforced Materials." *Composites: Part A 38*, 2007, pp. 2333-2341.
15. Lorriott, T.; Marion, G.; Harry, R.; and Wargnier, H.: "Onset of free-edge delamination in Composite Laminates Under Tensile Loading." *Composites Part B: Engineering*, Vol. 34, 2003, pp. 459-471.
16. Garg, C. A.: "Delamination—A Damage Mode in Composite Structures." *Engineering Fracture Mechanics*, Vol. 29, No. 5, 1988, pp. 557-584.

17. Tan, C. S.: *Stress Concentrations in Laminated Composites*." Technomic Publishing Company, Inc., 851 New Holland Avenue, Box 3535, Lancaster, Pennsylvania 17604.
18. Tao, J.; and Sun, C. T.: "Influence of Ply Orientation on Delamination in Composite Laminates." *Journal of Composite Materials*, Vol. 32, No.21, 1998, pp. 1933-1947.
19. Satyanarayana, A.; Bogert, P. B.; and Chunchu, P. B.: "The Effect of Delamination on Damage Path and Failure Load Prediction for Notched Composite Laminates." *Proceedings of the 48th AIAA/ASME/ASCE/AHS/ASC Structures, Structural Dynamics and Materials Conference*, April 2007, Honolulu, Hawaii, AIAA 2007-1993.
20. Bisagni, C.: "Progressive Delamination Analysis of Stiffened Composite Panel in Post-Buckling." *Proceedings of the 47th AIAA/ASME/ASCE/AHS/ASC Structures, Structural Dynamics and Materials Conference*, Newport, Rhode Island, May 2006, AIAA 2006-2178.
21. Yang, Q.; and Cox, B.: "Cohesive Models for Damage Evolution in Laminated Composites." *International Journal of Fracture*, 2005, pp. 107-137, doi: 10.1007/s10704-005-4729-6.
22. Guinard, S.; Allix, O.; Guedra-Degeorges, D.; and Vinet. A.: "A 3D Damage Analysis of Low-Velocity Impacts on Laminated Composites." *Composites Science and Technology*, Vol. 62, 2002, pp. 585-589.
23. Dávila, C. G.; Camanho, P. P.; and Turon, A.: "Effective Simulation of Delamination in Aeronautical Structures Using Shells and Cohesive Elements." *Journal of Aircraft,* Vol. 45, No. 2, 2008, pp. 663-672.
24. Green, G. G.; Wisnom, M. R.; and Hallett, S. R.: "An Experimental Investigation Into the Tensile Strength Scaling of Notched Composites." *Composites Part A: Applied Science and Manufacturing*, Vol. 38, No. 3, 2007, pp. 867-878, doi: 10.1016/j.compositesa.2006.07.008.
25. Hashin, Z.: "Failure Criteria for Unidirectional Fiber Composites." *Journal of Applied Mechanics*, Vol. 47, 1980, pp. 329-334.
26. Hashin, Z.; and Rotem, A.: "A Fatigue Failure Criterion for Fiber-Reinforced Composite Materials." *Journal of Composite Materials*, Vol. 7, October 1973, pp. 448-464.
27. Dávila, C. G.; Camanho, P. P.; and Rose, C. A.: "Failure Criteria for FRP Laminates." *Journal of Composite Materials*, Vol. 39, No. 4, 2005, pp. 323-345, doi: 10.1177/0021998305046452.
28. Dávila, C. G.; Camanho, P. P.; and de Moura, M. F.: "Mixed-Mode Decohesion Elements for Analyses of Progressive Delamination." *Proceedings of the 42nd AIAA/ASME/ASCE/AHS/ASC Structures, Structural Dynamics, and Materials Conference*, Seattle, Washington, April 2001, AIAA-2001-1486.
29. Goyal, V.; Johnson, E.; Dávila, C.; and Jaunky, N.: "An Irreversible Constitutive Law for Modeling the Delamination Process Using Interface Elements." *Proceedings of the 43rd AIAA/ASME/ASCE/AHS/ASC Structures, Structural Dynamics, and Materials Conference*, April 2002, AIAA-2002-1576.
30. Anon.: *ABAQUS™ User's Manual, Vol. 1-3, Version 6.5*. Hibbitt, Karlsson, and Sorensen, Pawtucket, Rhode Island, 2003.
31. Camanho, P. P.; Dávila, C. G.; Pinho, S. T.; Iannucci, L.; and Robinson, P.: "Prediction of in-Situ Strengths and Matrix Cracking in Composites under Transverse Tension and In-Plane Shear." *Composites Part A: Applied Science and Manufacturing*, Vol. 37, No. 2, 2006, pp. 165-176, doi: 10.1016/j.compositesa.2005.04.023.
32. Turon, A.; Dávila, C. G.; Camanho, P. P.; and Costa, J.: "An Engineering Solution for Mesh Size Effects in the Simulation of Delamination Using Cohesive Zone Models." *Engineering Fracture Mechanics*, Vol. 74, No. 10, 2007, pp. 1665-1682, doi: 10.1016/j.engfracmech.2006.08.025.

REPORT DOCUMENTATION PAGE

Form Approved
OMB No. 0704-0188

1. REPORT DATE *(DD-MM-YYYY)*	2. REPORT TYPE	3. DATES COVERED *(From - To)*
01-05-2010	Contractor Report	11-01-2008 to 11-01-2009

4. TITLE AND SUBTITLE
Predicting Failure Progression and Failure Loads in Composite Open-Hole Tension Coupons

5a. CONTRACT NUMBER
NNL07AA00B

5b. GRANT NUMBER

5c. PROGRAM ELEMENT NUMBER

6. AUTHOR(S)
Satyanarayana, Arunkumar; Przekop, Adam

5d. PROJECT NUMBER

5e. TASK NUMBER
NNL07AM32T

5f. WORK UNIT NUMBER
984754.02.07.07.15.04

7. PERFORMING ORGANIZATION NAME(S) AND ADDRESS(ES)
NASA Langley Research Center
Hampton, VA 23681-2199

8. PERFORMING ORGANIZATION REPORT NUMBER

9. SPONSORING/MONITORING AGENCY NAME(S) AND ADDRESS(ES)
National Aeronautics and Space Administration
Washington, DC 20546-0001

10. SPONSOR/MONITOR'S ACRONYM(S)
NASA

11. SPONSOR/MONITOR'S REPORT NUMBER(S)
NASA/CR-2010-216700

12. DISTRIBUTION/AVAILABILITY STATEMENT
Unclassified - Unlimited
Subject Category 39
Availability: NASA CASI (443) 757-5802

13. SUPPLEMENTARY NOTES
Langley Technical Monitor: Dawn C. Jegley

14. ABSTRACT

Failure types and failure loads in carbon-epoxy [45n/90n/-45n/0n]ms laminate coupons with central circular holes subjected to tensile load are simulated using progressive failure analysis (PFA) methodology. The progressive failure methodology is implemented using VUMAT subroutine within the ABAQUS™/Explicit nonlinear finite element code. The degradation model adopted in the present PFA methodology uses an instantaneous complete stress reduction (COSTR) approach to simulate damage at a material point when failure occurs. In-plane modeling parameters such as element size and shape are held constant in the finite element models, irrespective of laminate thickness and hole size, to predict failure loads and failure progression. Comparison to published test data indicates that this methodology accurately simulates brittle, pull-out and delamination failure types. The sensitivity of the failure progression and the failure load to analytical loading rates and solvers' precision is demonstrated.

15. SUBJECT TERMS
Brittle; Composites; Graphite-epoxy; Progressive failure

16. SECURITY CLASSIFICATION OF:			17. LIMITATION OF ABSTRACT	18. NUMBER OF PAGES	19a. NAME OF RESPONSIBLE PERSON
a. REPORT	b. ABSTRACT	c. THIS PAGE			STI Help Desk (email: help@sti.nasa.gov)
					19b. TELEPHONE NUMBER *(Include area code)*
U	U	U	UU	60	(443) 757-5802